This version of the article has been accepted for publication, after peer review (when applicable) and is subject to Springer Nature's AM terms of use, but is not the Version of Record and does not reflect post-acceptance improvements, or any corrections. The Version of Record is available online at: https://doi.org/10.1007/s10035-015-0546-4
Postprint of: Nitka M., Tejchman J., Modelling of concrete behaviour in uniaxial compression and tension with DEM, Granular Matter, Vol. 17 (2015), pp. 145–164

Modelling of concrete behaviour in uniaxial compression and tension with DEM

M. Nitka and J. Tejchman
Gdańsk University of Technology
80-233 Gdańsk-Wrzeszcz, Narutowicza 11/12, Poland
micnitka@pg.gda.pl, tejchmk@pg.gda.pl

Abstract

The paper focuses on the discrete modelling of the behaviour of plain concrete during uniaxial compression and uniaxial tension using the discrete element method (DEM). The model takes into account the concrete heterogeneity at the meso-scale level. The effect of concrete density, size of aggregate grains and specimen size on the stress-strain curve, volume changes and fracture process is studied. In addition, the evolution of contact forces, grain rotations, displacement fluctuations and strain localization during deformation is investigated. The elastic, kinetic, plastic and numerical dissipated energy is calculated and analysed at a different stress-strain stage. Concrete is described as a one-phase or three-phase material. Discrete macroscopic 2D and 3D results are compared with corresponding experiments. A satisfactory agreement between experiments and calculations is achieved.

Keywords: plain concrete, DEM, fracture, micro-structure, strain localization

1. Introduction

Fracture (cracking process) is a fundamental phenomenon in quasi-brittle and brittle materials [1]-[3] (i.e. in materials which break without significant deformation when subjected to stress). It is a major reason of mechanical damage under loading that contributes to a significant degradation (reduction) of the material strength. It is highly complex due to a heterogeneous structure of brittle materials over many different length scales, changing in e.g. concrete from a few nanometers (hydrated cement) to the millimetres (aggregate particles). Therefore, the material heterogeneity should be taken into account when realistically modelling the material behaviour. An understanding of a fracture process is of major importance to ensure safety of the structure and to optimize the behaviour of material.

During a damage process, micro-cracks first arise in a hardening region before the peak on the stress-strain curve which change gradually during material softening into dominant distinct macroscopic cracks up to rupture [3]. Thus, a mechanical damage process is generally subdivided into two main stages: appearance of narrow regions of intense deformation (equivalent to the region of intense micro-cracking) ahead of macro-cracks and occurrence of discrete macro-cracks. A realistic description of localized zones (called also fracture process zones FPZs) in concrete (their width, length, shape and distance), which are not negligibly small as compared to the specimen size [1] and is of a particular major importance to understand concrete degradation and to determine a combined deterministic-statistical size effect. It is also extremely important to determine a characteristic length of micro-structure in continuum crack models for cementation materials and a transition phase in coupled continuous-discontinuous crack approaches [3]. This length is introduced into continuum models via e.g. non-local or strain-gradient theories to properly describe the size and spacing of localized zones, to obtain mesh-independent finite element results and to capture a deterministic size effect [1], [3], [4].

At the meso-scale, concrete may be considered as a composite material by distinguishing three important phases: cement matrix, aggregate and interfacial transition zones ITZs wherein [2], [5], [6]. In particular, the presence of aggregate and ITZs is important since the volume fraction of aggregate can be as high as 70-75% in concrete and ITZs with the thickness of about 50 μm are always the weakest regions in usual concretes [2] wherein cracking starts (because of their higher porosity). The advantage of meso-scale modelling is the fact that it directly simulates micro-structure and can be used to comprehensively study local phenomena at the micro-level such as the mechanism of the initiation, growth and formation of localized zones and cracks which affect the macroscopic concrete behaviour (the concrete behaviour at the meso-scale fully determines the macroscopic non-linear behaviour [1]). Thus, the mesoscopic results allow for a better calibration of continuous and discontinuous constitutive continuum models and an optimization design of concrete with enhanced strength and ductility. Discrete models (if they are enough consistent) might progressively replace experimental tests to study the influence of the concrete mesostructure (aggregates size, aggregates volume/mortar volume, macro porosity, etc.) on the concrete behaviour. The disadvantages are: enormous computational cost, inability to model aggregate shape accurately and difficult calibration procedure. In addition, it is difficult to assume geometric and mechanical properties of ITZs for concrete considered as a 3-phase body.

The concrete behaviour at the meso-scale can be described with continuum models [5]-[8] and discrete models [2], [9], [10]. In this study we used a discrete approach. Within discrete methods,

the most popular ones are: a classical particle DEM [11]-[17], interface element models with constitutive laws based on non-linear fracture mechanics [18], [19] and lattice methods [2], [10], [20-29].

In the paper, in order to develop an understanding of the failure process of plain concrete at the aggregate scale, the discrete element method (DEM) was used [14], [30]. In DEM a mechanical response of materials is governed by interactions at contacts between constituent particles and between particles and boundaries being responsible for the emergent complexity of phenomena occurring in these materials. In order to reproduce the concrete behaviour, a three-dimensional spherical discrete element model YADE was used, which was developed at University of Grenoble [31], [32]. The model was successfully used for describing the behaviour of different engineering materials with a granular structure (mainly of granular materials by taking shear localization into account [33]-[35]). In the first research step, the concrete behaviour was investigated during simple quasi-static uniaxial tests without confining pressure (compression and tension). Our main aim was to check the capability of DEM to simulate fracture in concrete. Concrete was considered as a one-phase and three-phase material by taking breakable cohesive inter-particle bonds between particles. The process of strain localization and cracking were studied in detail. The effect of material density, size and grain distribution of aggregate and specimen size on the behaviour of concrete on stress-strain curve, volume change and fracture was shown. In addition, the evolution of contact forces, rotations, displacement fluctuations and porosity at the aggregate level during deformation was studied. The width of a localized zone was determined based on grain displacements and compared with the width of a damage zone based on broken contacts. Every kind of energy was calculated and analysed at different stress–strain stages. Discrete results at global level were compared with corresponding experiments. Since the concrete micro-structure in experiments was not precisely known, the numerical quasi-static simulations were mainly carried out under 2D stress conditions with the one-phase concrete model in order to significantly shorten the computation time. Only one 3D simulation for tension and compression was performed. However, the effect of the different parameters on the global behaviour of concrete was qualitatively similar in the 2D and 3D concrete models. The originality of this work comes from 3 points: 1) DEM calculations of concrete as a three-phase material, 2) analyses of micro-structural events (force chains, displacement fluctuations, grain rotations, local porosity change, strain localization, damage zones) at the aggregate level, and c) a determination of the width of localized zones based on resultant grain displacements in concrete.

In the research literature different discrete models have been developed for cohesive soils and quasi-brittle materials that differ besides the used bonding concept in dimensionality, particle shape and particle arrangement (e.g. [14], [15], [36]-[39]). They were mainly used to study the behaviour of cohesive materials at the global scale. Our discrete model with linear normal contacts between spherical aggregate and cement particles was intended as a minimum discrete model in terms of restricted inter-particle motions, bond contact and particle shape and particles' amount in order to capture both the macroscopic and mesoscopic behaviour of concrete. In addition, a simple construction method of the discrete element assembly was used to create the initial structure of concrete specimens.

2. Discrete Element Method

In order to study the evolution of micro-structure in plain concrete during fracture (strain localization and cracking propagation), a three-dimensional spherical discrete element model YADE [31], [32] was used. The model takes advantage of the so-called soft-particle approach (i.e. the model allows for particle deformation which is modelled as an overlap of particles). A linear normal contact model under compression was used. The algorithm used in YADE involves two steps. In the first one, interaction forces were computed when elements slightly interpenetrate each other (penetration below 10% of the radius). In the second step, Newton second law was used to compute, for each element, the resulting acceleration, which was then time integrated to find the new element position. This process was repeated until the simulation was finished. The dynamic formulation allowed the model for following highly non-linear behaviour characteristic of concrete in both: a tensile and shear failure mode. To maintain the numerical stability of the method and to obtain a quick convergence to a quasi-static state of equilibrium of the assembly of particles, damping forces were introduced. For the sake of simplicity, the aggregate and cement matrix particles in concrete were exclusively modelled as pure interacting spheres. The interaction force vector $\vec{F}$ representing the action between two spherical discrete elements in contact was decomposed into a normal and tangential vector, respectively. The normal forces acting on spheres were modelled by an elastic law with cohesion. The normal and tangential forces were linked to the displacements through the normal stiffness K_n and the tangential stiffness K_s (Figs.1a-1c)

$$\vec{F}_n = K_n U \overrightarrow{N}, \tag{1}$$

$$\vec{F}_s = \vec{F}_{s,prev} + K_s \Delta \vec{X}_s, \tag{2}$$

where U is the overlap between spheres, $\vec{N}$ denotes the normal vector at the contact point, $\Delta \vec{X}_s$ is the incremental tangential displacement and $\vec{F}_{s,prev}$ is the tangential force from the previous iteration.

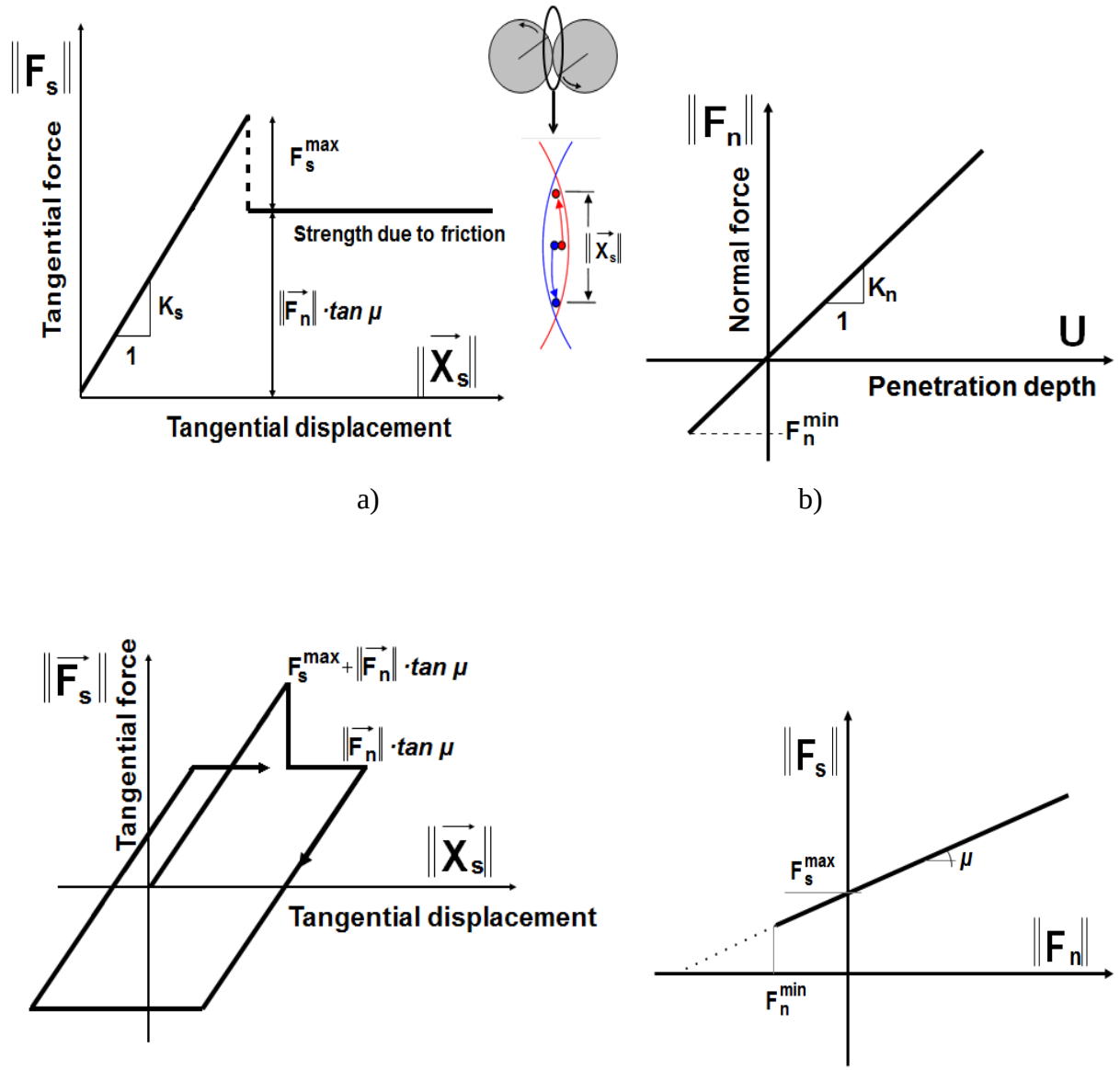

Figure 1: Mechanical response of DEM: a) tangential contact model, b) normal contact model, c) loading and unloading path in tangential contact model and d) modified Mohr-Coulomb model [31], [32]

The stiffness parameters were computed with the aid of the modulus of elasticity of the grain contact E_c and two neighbouring grain radii R_A and R_B (to determine the normal stiffness K_n) and with the aid of the modulus of elasticity E_c and Poisson's ratio ν_c of the grain contact and two neighbouring grain radii R_A and R_B (to determine the tangential stiffness K_s), respectively [31], [32]

$$K_n = E_c \frac{2R_A R_B}{R_A + R_B} \quad \text{and} \quad K_s = \nu_c E_c \frac{2R_A R_B}{R_A + R_B}. \tag{3}$$

If the grain radius $R_A = R_B = R$, the stiffness parameters were equal to: $K_n = E_c\, R$ and $K_s = \nu_c\, E_c\, R$, respectively (thus $K_s/K_n = \nu_c$). The contact forces $\vec{F}_s$ and $\vec{F}_n$ satisfied the cohesive-frictional Mohr-Coulomb equation (Fig.1c)

$$\left\|\vec{F}_s\right\| - F_{max}^s - \left\|\vec{F}_n\right\| \times \tan\mu \leq 0 \text{ (before contact breakage)}$$

and

$$\left\|\vec{F}_s\right\| - \left\|\vec{F}_n\right\| \times \tan\mu \leq 0, \text{ (after contact breakage)}, \tag{4}$$

where μ denotes the inter-particle friction angle and $\vec{F}_{max}^s$ is the cohesive force between spheres. The normal force might be negative down to the minimum value of F_n^{min} if there was no a geometrical contact between spheres. If this minimum normal force between spheres F_n^{min} was reached, the contact was broken. Moreover, if any contacts between grains re-appeared, cohesion between them was not taken into account. A crack was considered as open if cohesive forces between grains disappeared when a critical threshold was reached. The movement of fragments (mass-spring systems with cohesion) was similar to the rigid body movement [32].

A choice of a very simple linear elastic normal contact was intended to capture on average various contact possibilities in real concrete. One assumed that the cohesive force and tensile force were a function of the cohesive stress C (maximum shear stress at pressure equal to zero), tensile normal stress T and sphere radius R [31]

$$F_{max}^s = C \times R^2 \quad \text{and} \quad F_{min}^n = T \times R^2 . \tag{5}$$

For two spheres in contact, the smaller values of C, T and R were assumed. To dissipate excessive kinetic energy in a discrete system, a simple local non-viscous damping scheme was adopted [40] which assumed a change of forces by using the damping parameter α

$$F_{adpt}^{k} = F_{resg}^{k}\left(1 - \alpha \cdot \mathrm{sgn}\left(v_{adpt}^{k} \cdot F_{resg}^{k}\right)\right), \tag{6}$$

where $\vec{F}^k$ and $\vec{v}^k$ are the k^{th} components of the residual force and translational velocity, respectively. A positive damping coefficient α is smaller than 1 (sgn(•) returns the sign of the k^{th} component of velocity). The equation can be separately applied to each k-th component of a 3D

vector *x*, *y* and *z*. The following five main local material parameters were needed for our discrete simulations: E_c, ν_c, μ, F_n^{min} and F_s^{max} which were calibrated with real laboratory uniaxial tests on compression by van Mier [41] and tension by van Vliet and van Mier [42] of concrete specimens. In addition, the particle radius *R*, particle mass density ρ and damping parameters α were required. We did not increase the rolling resistance of pure spheres by including contact moments in order to decrease the material brittleness [33], [34] since the effect of contact moments was not significant due to fact that the aggregate rotations in concrete were very small during cracking (see Fig.18). Note that for higher stress states, our model will have to probably include grain crushing and more complex contact laws [43], [44].

3. Discrete results at macro-level

The numerical quasi-static simulations of uniaxial compression and uniaxial tension were carried out mainly under 2D stress conditions with one-phase concrete model in order to simplify calculations and to shorten their time (only one 3D simulation was carried out for comparative reasons). Qualitatively the effect of the different parameters on the global behaviour of concrete was similar as in the 3D three-phase concrete model. In the 2D simulations, the specimen depth was always equal to the sphere diameter *d* (i.e. only grain layer was simulated in a perpendicular plane) and the discrete calculations were carried out as for cylinders (instead of spheres). In the laboratory experiments, the following aggregate size was used: d_{min}≤0.125 mm and d_{max}=16 mm (uniaxial compression [41]) and d_{min}=0.25 mm and d_{max}=8 mm (uniaxial tension [42]). In the simulations for the simplicity, the spheres were assumed to approximately simulate both aggregate and cement matrix. They had the different diameter *d*, varying between d_{min}=0.125-2 mm (lower bound) and d_{max}=12 mm (upper bound). The maximum sphere diameter d_{max} was assumed as the mean value from laboratory tensile and compressive tests to simulate the behaviour of the same concrete under two different stress conditions (compression and tension). The mean sphere diameter was always d_{50}=2 mm. Thus, the sphere distribution curve included solely the linear sections between d_{50} and d_{max} and between d_{min} and d_{50}. For the sake of simplicity, the entrapped air in macro-pores of concrete was not taken into account (note that the micro-porosity between grains cannot be considered as the macro-porosity). The modulus of elasticity E_c and Poisson's ratio ν_c of spherical contacts were taken as E_c=15 GPa and ν_c=0.2 (Eq.3), respectively. The values of *C* and *T* (Eq.5) were chosen as 140 MPa and 25 MPa, respectively. The mass density was ρ=2500 kg/m^3 and the inter-particle friction angle was μ=30^o

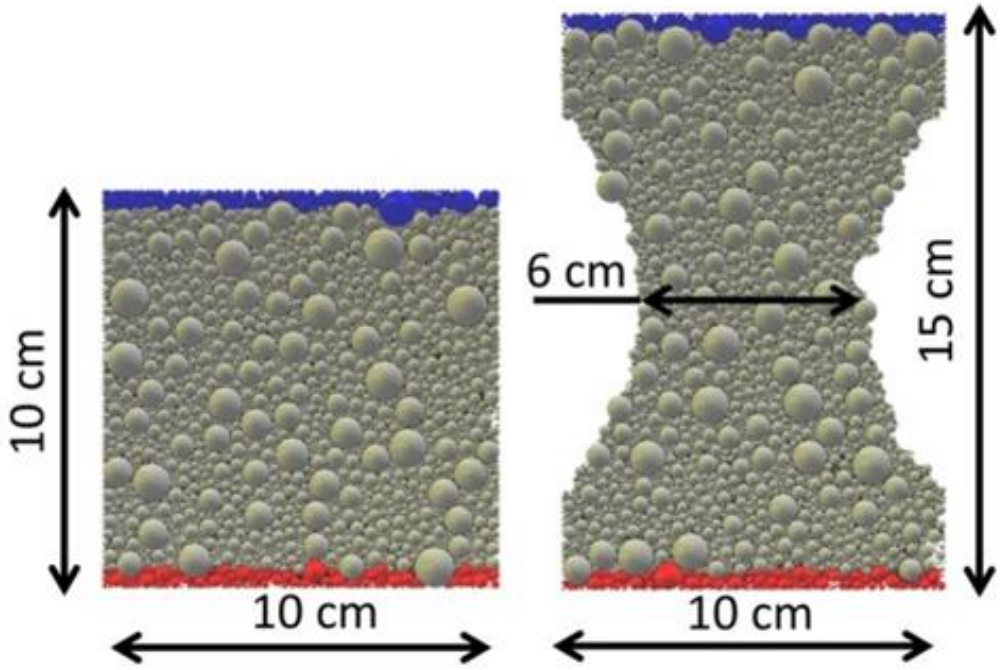

a) b)

Figure 2: Concrete specimens with stochastically distributed spheres between smooth rigid boundaries for discrete simulations of uniaxial compression (a) and uniaxial tension (b) following laboratory tests by van Vliet and van Mier [41], [42]

For uniaxial compression 2D tests [41], the quadratic specimen 0.1×0.1 m^2 (Fig.2a) was assumed and for uniaxial tension tests [42], a so called 'dog-bone' shape was chosen: the height 0.15 m, width 0.10 m along the top and bottom and 0.06 m at the mid-height (Fig.2b). Some grain layers at the top and bottom of the concrete specimens were used to simulate steel plates in the loading machine. The top and bottom boundaries could freely move in a horizontal direction and the bottom was fixed in a vertical direction. Thus, the both horizontal boundaries were assumed to be ideally smooth (as in experiments). The effect of the wall roughness on the results (that is known to have a big impact [41]) was not investigated (page 6). Next, a constant velocity was applied to the grains along the top boundary to induce tensile or compressive deformation. Due to the information lack on the internal structure of test specimens [41], [42], each concrete assembly was constructed in a very simple way by putting spheres of a different diameter into a concrete specimen at random according to linear grain distribution curves (with the inter-granular friction equal μ=0 in order to obtain a relatively dense specimen). The assembly was then allowed to settle to a state when the kinetic energy was negligible and then all contact forces between spheres were deleted. Next, the parameter μ was set to its final value of μ=30º. Afterwards the assembly was subjected to the upper boundary driven compression or tension. The particle packing was random and thus was slightly different during each new specimen construction. The particle packing slightly (less than 10%) affected the results using the same

grain distribution curve. During the tests, the prescribed vertical strain rate was slow enough ($\dot{\varepsilon} = 10^{-3}$ [1/s]) in order to ensure the test was conducted in quasi-static conditions (see Fig.5A). Due to this simple method, the initial coordination number (average number of contacts at the single particle) was relatively high [45]: 5-6 (2D calculations) and 11 (3D calculations). The damping parameter was always chosen as α=0.08 (Eq.6). In the case of α<0.08 too excessive kinetic energy was always created during fracture (the tensile numerical test could not be performed without numerical damping due to excessively high velocities of particles). In turn, the effect of the α-value on global results for $\alpha \geq 0.08$ became smaller (see Fig.5B).

Effect of initial specimen density (2D analyses)

In all concrete specimens, 75% of their volume was filled in with the spheres of the diameter $d \geq 2$ mm which simulated aggregate particles. Next, the spheres with the diameter below d<2 mm (which corresponded to the cement matrix) were added to reach the total sphere volume ratio $V_1=V_s/V$ (V_s - the sphere volume and V – the specimen volume): V_1=75%-125%. At V_1=100% and V_1=125% some overlaps between spheres obviously occurred (the initial internal forces were removed). The total sphere volume ratio indirectly corresponds to porosity in granulates ($n=V_p/V$, where $V_p=V-Vs$ - the volume of void-space) and can be considered as a physical parameter for the given concrete. The total number of spheres was 3617-11168 (uniaxial compression) and 4537-13193 (uniaxial tension). The maximum sphere diameter was taken as d_{max}=12 mm and the minimum sphere diameter as d_{min}=1 mm. The calculation time for the uniaxial test was 8-12 hours on PC 2.7 MHz.

The calculated vertical normal stress σ_y versus the vertical normal strain ε_y for uniaxial compression was shown in Fig.3A as compared to experiments [41] and for uniaxial tension in Fig.3B as compared to experiments [42] for d_{50}=2 mm. The denser the specimen, the higher was apparently the concrete initial stiffness and strength and smaller was the material ductility. As compared to the experiments, the calculated material response of 2D concrete specimens was always too brittle. The results of the global modulus of elasticity E , compressive strength f_c and tensile strength f_t with V_1=90% (E=30 GPa, f_c=43 MPa, f_t=4.5 MPa) corresponded well to the experimental results (E=30 GPa, f_c=43 MPa, f_t=2.7 MPa). The modulus of elasticity E was connected directly with the modulus of elasticity of the grain contact $E \cong 2E_c$ (Fig.4).

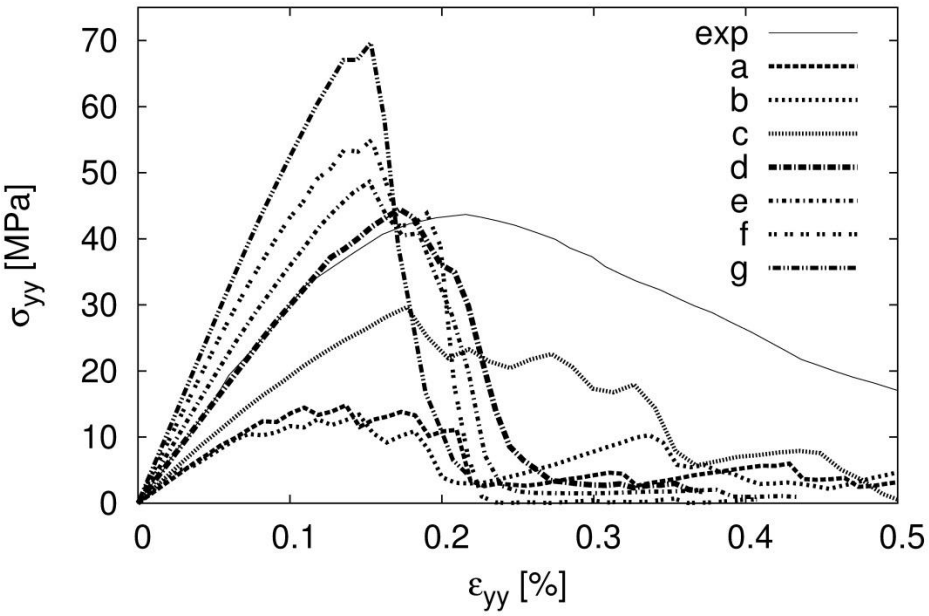

a) V_1=75%, b) V_1=80%, c) V_1=85%, d) V_1=90%, e) V_1=95%, f) V_1=100% and g) V_1=125%

A)

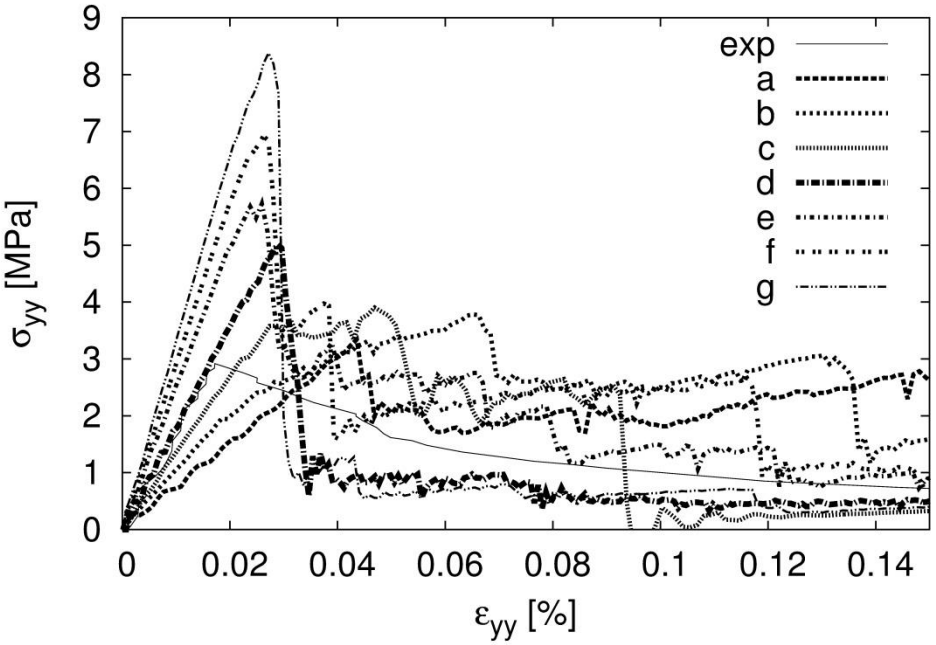

a) V_1=75%, b) V_1=80%, c) V_1=85%, d) V_1=90%, e) V_1=95%, f) V_1=100% and g) V_1=125%

B)

Figure 3: Calculated stress-strain σ_y-ε_y curves during uniaxial compression (A) and uniaxial tension (B) for 2D concrete specimens (d_{min}=1 mm, d_{50}=2 mm, d_{max}=12 mm and with 7 different sphere volume ratio V_1: a) V_1=75%, b) V_1=80%, c) V_1=85%, d) V_1=90%, e) V_1=95%, f) V_1=100% and g) V_1=125% ('exp' – experiments by van Vliet and van Mier [41], [42])

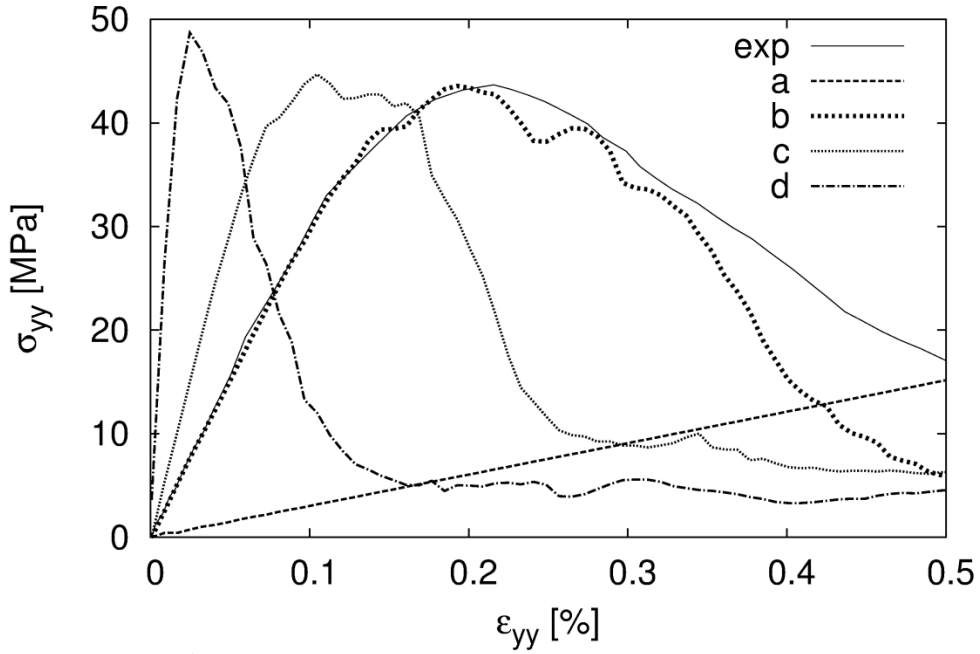

a) E_c=1.5 GPa, b) E_c=15 GPa, c) E_c=30 GPa and d) E_c=150 GPa

A)

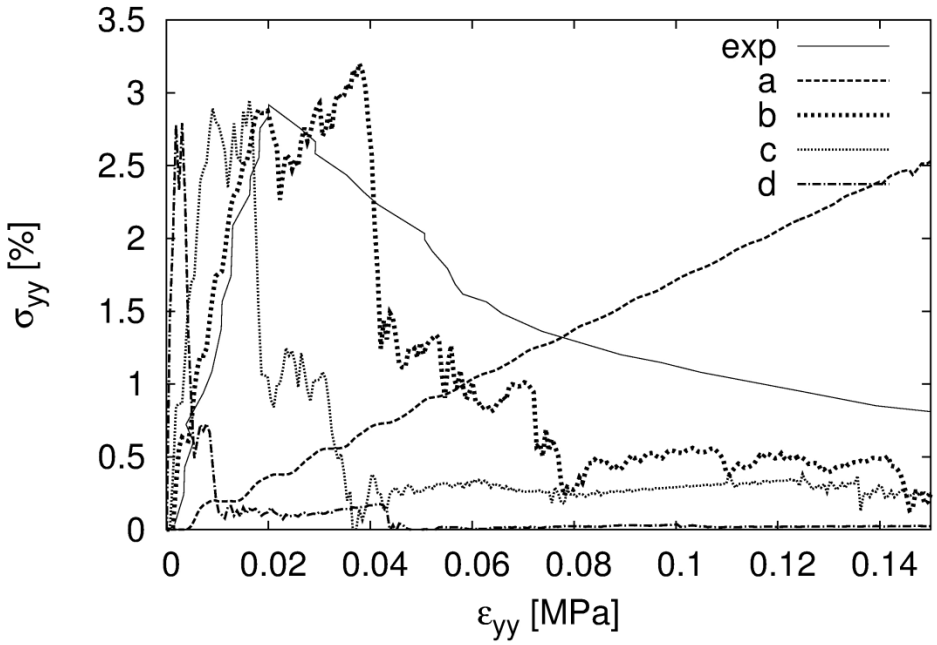

a) E_c=1.5 GPa, b) E_c=15 GPa, c) E_c=30 GPa and d) E_c=150 GPa

B)

Figure 4: Calculated stress-strain σ_y-ε_y curves during uniaxial compression (A) and uniaxial tension (B) for 2D concrete specimens (d_{min}=1 mm, d_{50}=2 mm, d_{max}=12 mm and V_1=90%) with different normal contact modulus of elasticity E_c: a) E_c=1.5 GPa, b) E_c=15 GPa, c) E_c=30 GPa and d) E_c=150 GPa ('exp' – experiments by van Vliet and van Mier [41], [42])

Figure 5 shows the effect of the prescribed strain rate along the specimen top $\dot{\varepsilon}$ and damping parameter α on the stress-strain diagram during uniaxial compression. For $\dot{\varepsilon} < 10^{-2}$ 1/s (Fig.5A) and $\propto = 0.08$ (Fig.5B) the material response was similar and could be treated as quasi static.

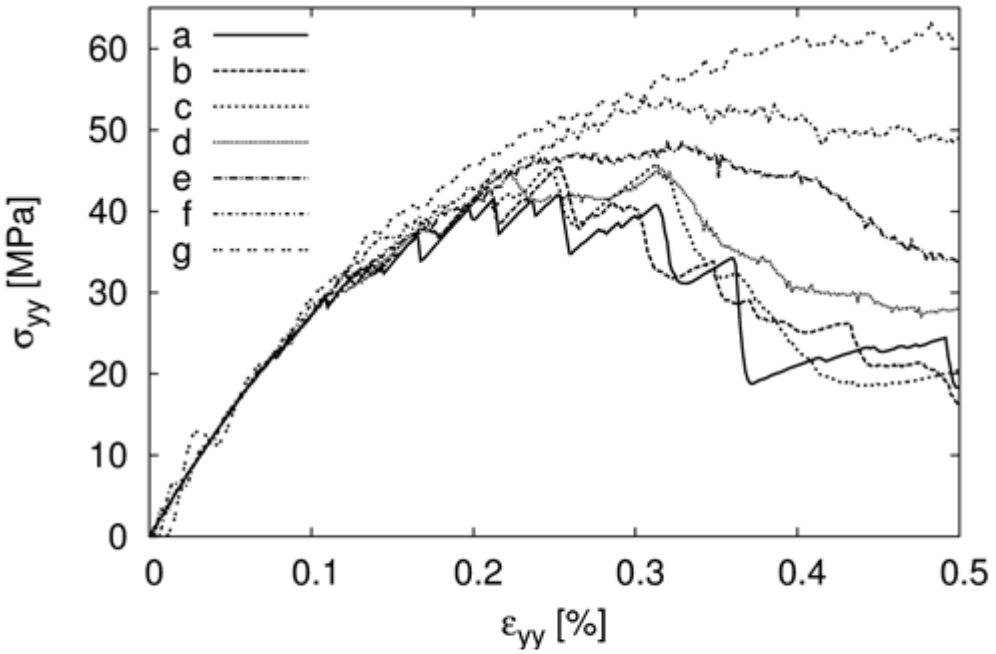

a) $\dot{\varepsilon} = 10^{-5}$ 1/s, b) $\dot{\varepsilon} = 10^{-4}$ 1/s, c) $\dot{\varepsilon} = 10^{-3}$ 1/s, d) $\dot{\varepsilon} = 10^{-2}$ 1/s,
e) $\dot{\varepsilon} = 2 \times 10^{-2}$ 1/s, f) $\dot{\varepsilon} = 10^{-1}$ 1/s and g) $\dot{\varepsilon} = 2 \times 10^{-1}$ 1/s

A)

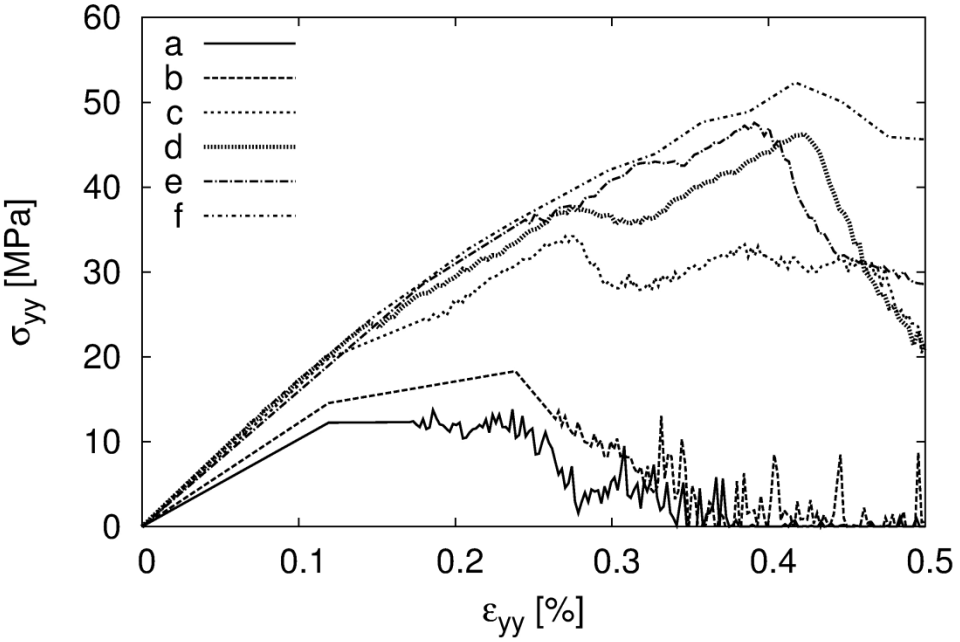

a) $\propto = 0$, b) $\propto = 0.01$, c) $\propto = 0.05$,
d) $\propto = 0.08$, e) $\propto = 0.1$ and f) $\propto = 0.2$

B)

Figure 5: Calculated stress-strain σ_y-ε_y curves during uniaxial compression for 2D concrete specimens (d_{min}=1 mm, d_{50}=2 mm, d_{max}=12 mm and V_1=90%): A) effect of different prescribed strain rate (α=0.08): a) $\dot{\varepsilon} = 10^{-5}$ 1/s, b) $\dot{\varepsilon} = 10^{-4}$ 1/s, c) $\dot{\varepsilon} = 10^{-3}$ 1/s, d) $\dot{\varepsilon} = 10^{-2}$ 1/s, e) $\dot{\varepsilon} = 2 \times 10^{-2}$ 1/s, f) $\dot{\varepsilon} = 10^{-1}$ 1/s and g) $\dot{\varepsilon} = 2 \times 10^{-1}$ 1/s and B) effect of damping parameter ($\dot{\varepsilon}$=10^{-3} 1/s): a) $\propto = 0$, b) $\propto = 0.01$, c) $\propto = 0.05$, d) $\propto = 0.08$, e) $\propto = 0.1$ and f) $\propto = 0.2$

Effect of minimum sphere size (2D analyses)

The minimum sphere diameter was varied: d_{min}=1.0 mm, d_{min}=0.5 mm and d_{min}=0.25 mm (with d_{50}=2 mm, d_{max}=12 mm and V_1=90%). The sphere number was 3’992, 8’791 and 23’488 during compression (with the coordination number equal to 5.1, 5.3 and 5.8) and 4’935, 10’949 and 28'862 during tension (with the coordination number equal to 5.0, 5.4 and 5.8), respectively.

The stress-strain curves indicated that the smaller the minimum sphere size d_{min} during compression was, the concrete strength f_c remained the same, but the brittleness and pre-peak non-linearity were smaller (Fig.6A). However, during tension (Fig.6B), the material ductility was insensitive to d_{min}, but the tensile strength f_t was higher with increasing d_{min} due to the effect of the larger mean grain size which contributed to a wider localized tensile zone and a size effect [3], [6]. The calculated initial stiffness and strengths for d_{min}=0.25 mm were in agreement with the experiments but the 2D post-peak responses were again too brittle. The calculation time with the smallest sphere diameter was 72 hours on PC.

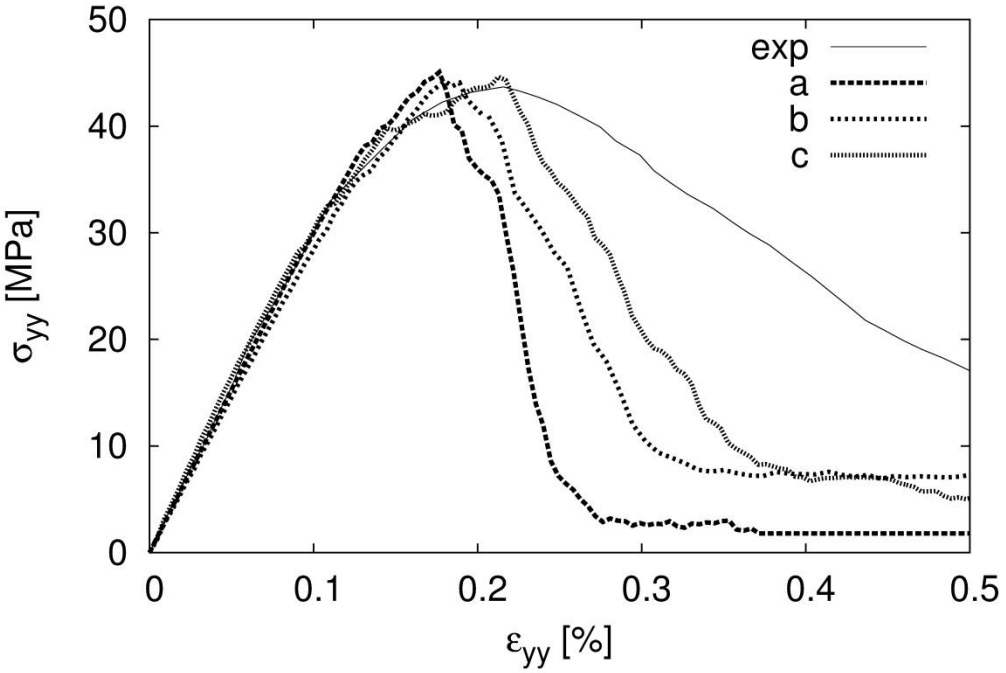

a) d_{min}=1 mm, b) d_{min}=0.5 mm and c) d_{min}=0.25 mm

A)

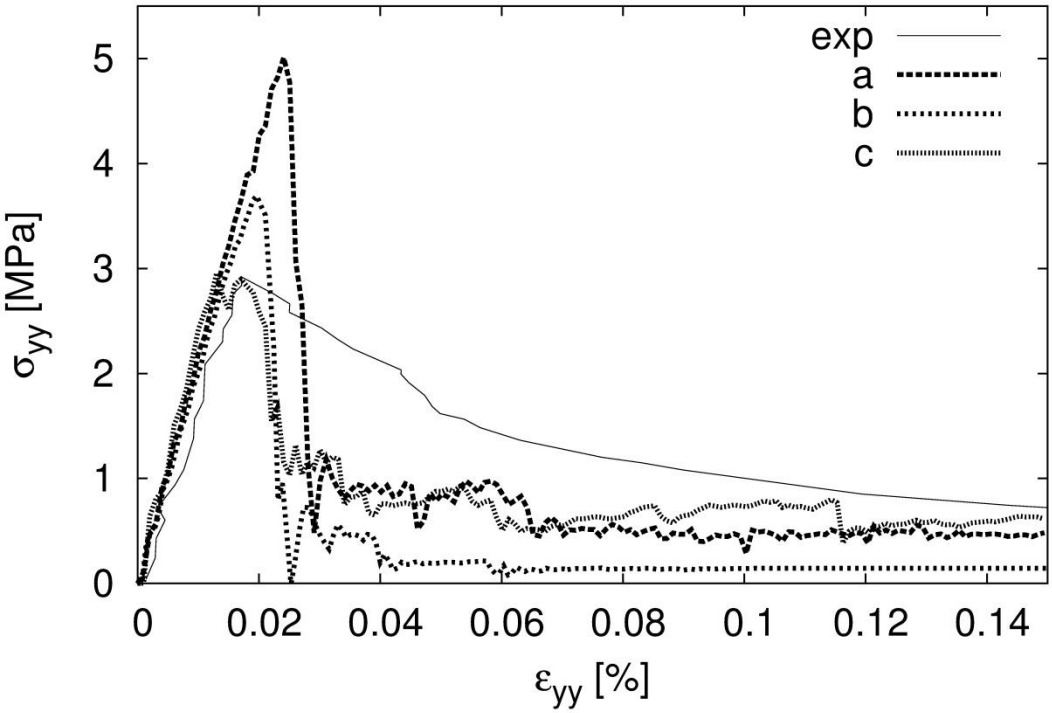

a) d_{min}=1 mm, b) d_{min}=0.5 mm and c) d_{min}=0.25 mm

B)

Figure 6: Calculated stress-strain σ_y-ε_y curves during uniaxial compression (A) and uniaxial tension (B) for 2D concrete specimens (d_{50}=2 mm, d_{max}=12 mm and V_1=90%) with different minimum sphere diameter d_{min}: a) d_{min}=1 mm, b) d_{min}=0.5 mm and c) d_{min}=0.25 mm ('exp' – experiments by van Vliet and van Mier [41], [42])

In Fig.7 the evolution of the global void ratio $e=V_p/V_s$ is shown (V_p – micro-pore area between grains and V_s - solid area (aggregate and cement matrix area). In order to exactly determine the area of micro-pores, the specimen was divided into very small squares. During uniaxial compression (Fig.7a), first insignificant contractancy and then after peak strong dilatancy appeared in the concrete specimen. For uniaxial tension (Fig.7b) global dilatancy occurred only in the concrete material.

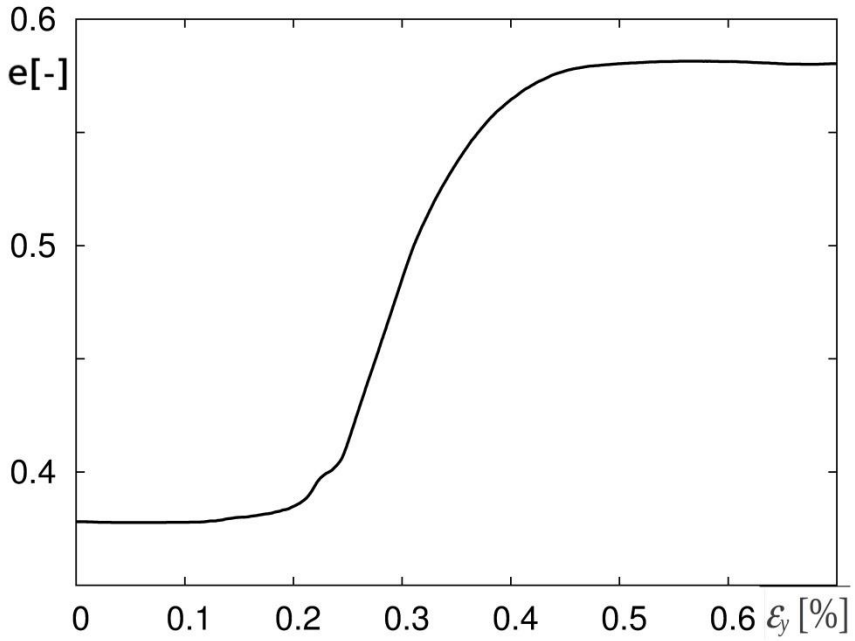

a)

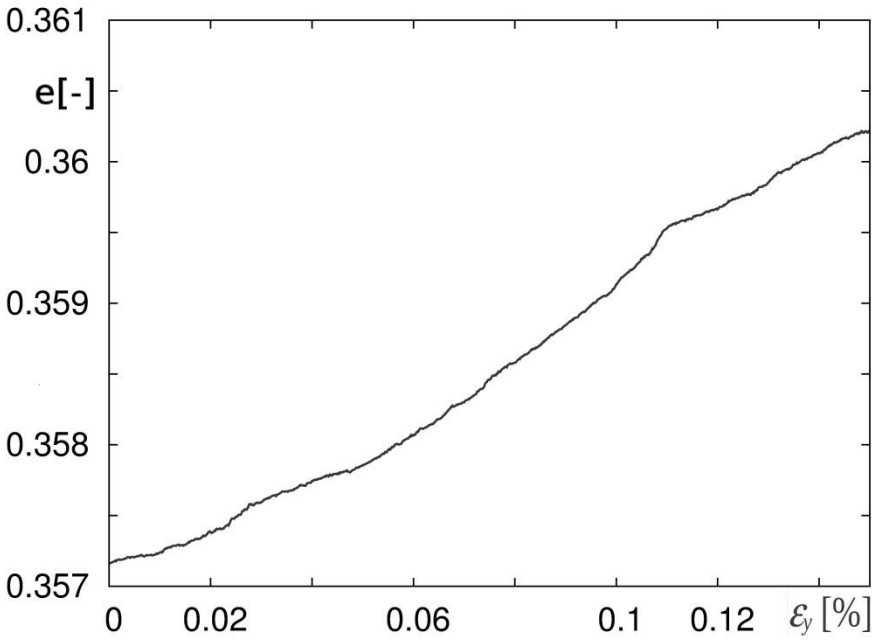

b)

Figure 7: Evolution of global void ratio *e* in 2D concrete specimens from DEM (1-phase material, d_{max}=12 mm, d_{min}=0.5 mm, d_{50}=2 mm and V_1=90%): a) uniaxial compression and b) uniaxial tension

Effect of specimen height during tension (2D analyses)

The calculations were carried out with geometrically similar concrete specimens under tension according to experiments by van Vliet and van Mier [42] (Fig.8). The specimen height varied between 0.075-0.6 m (d_{min}=0.5 mm, d_{50}=2 mm, d_{max}=12 mm and V_1=90%) (Fig.8).

The simulation results of Fig.8 showed that the tensile strength increased with decreasing height (as in the experiment [42]). It was higher by 60% for the smallest specimen as compared to the biggest one (similarly as in the laboratory test [42], i.e. 50%). However, the softening rate did not increase with the height (as in real tests).

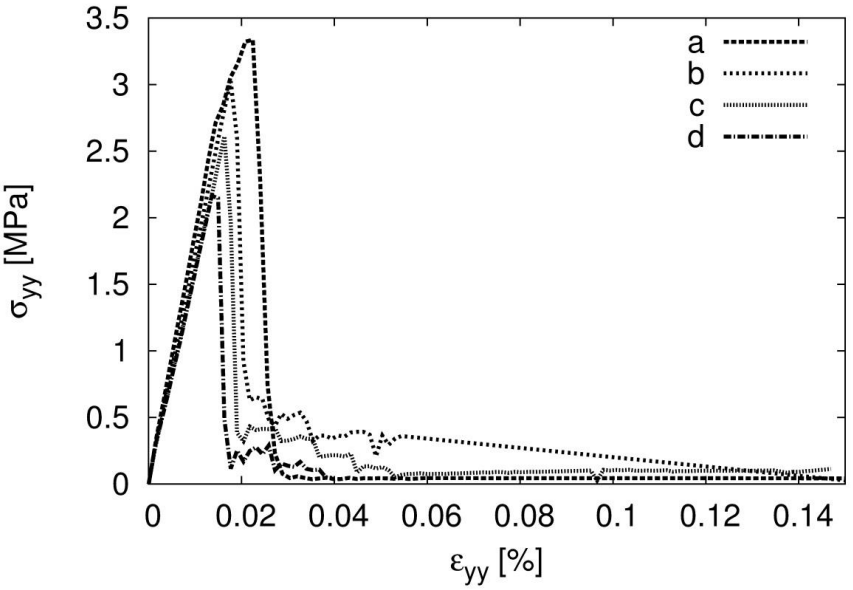

a) h=75 mm, b) h=150 mm, c) h=300 mm and d) h=600 mm

A)

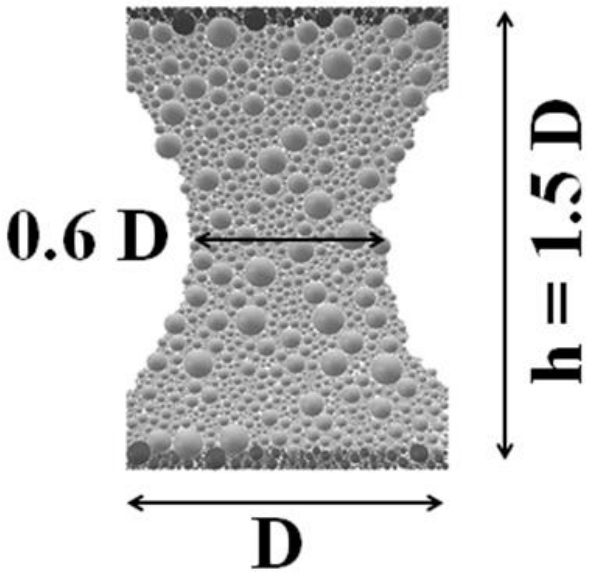

B)

Figure 8: Calculated stress-strain σ_y-ε_y curves (A) during uniaxial tension with different specimen height (B) for 2D concrete specimens: a) h=75 mm, b) h=150 mm, c) h=300 mm and d) h=600 mm (d_{min}=1 mm, d_{50}=2 mm, d_{max}=12 mm, V_1=90%, h=1.5D)

Effect of specimen depth (3D analyses)

The 3D calculations were carried out with the specimen depth of t=10 cm as in experiments (d_{max}=12 mm, d_{min}=1.0 mm, d_{50}=2 mm and V_1=90%), Fig.9. During compression (Fig.9A), the specimen included 291'577 spheres (the initial coordination number was n=11). In the case of tension (Fig.9B), 337'982 spheres were used (n=10.7). The calculation time was extremely long, i.e. 30 days.

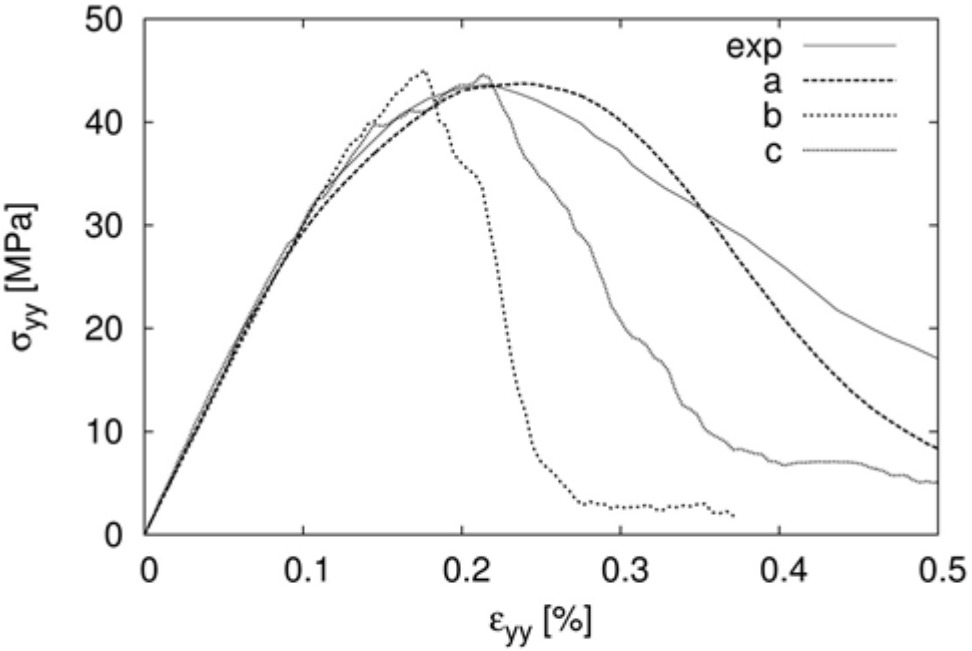

A)

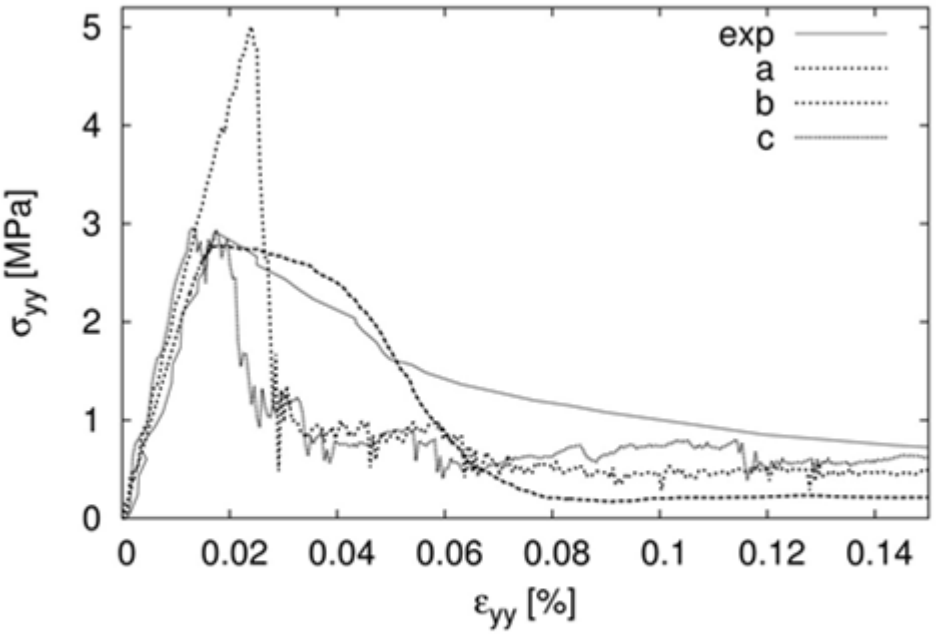

a) 2D results with d_{min} = 1.0 mm,
b) 2D results with d_{min} = 0.25 mm,
c) 3D results with t = 100 mm and d_{min} = 1.0 mm

B)

Figure 9: Calculated stress-strain σ_y-ε_y curves during uniaxial compression (A) and uniaxial tension (B) (d_{max}=12 mm, d_{50}=2 mm and V_1=90%): a) 2D results with specimen depth t=d with d_{min} = 1mm, b) 2D results with specimen depth t=d with d_{min}=0.25 mm and c) 3D results with t=100 mm and d_{min}=1.0 mm ('exp' – experiments by van Vliet and van Mier [41], [42])

In the 3D simulations as compared to the 2D ones, the material response became more ductile and stress fluctuations were significantly smaller due to a higher coordination number. The 3D stress-strain curves were also closer to the experimental ones both for compression and tension than the 3D outcomes (Fig.3). These results showed that 3D results were more realistic than the 2D results and the effect of the third dimension of micro-structure was pronounced.

Effect of three phases (2D analyses)

Concrete included 3 different phases: aggregate, cement matrix and interfacial transitional zones (ITZs) analogously as in lattice models [2], [28] (Fig.10) with d_{max}=12 mm, d_{min}=0.5 mm, d_{50}=2 mm and V_1=90%. The interfacial transition zone (ITZ) is a special region of the cement paste around particles which is perturbed by their presence [46]-[48]. Its origin lies in the packing of the cement grains against the much larger aggregate which leads to a local increase in porosity (micro-voids) and a presence of smaller cement particles. A paste with lower *w/c* (higher packing density) or made with finer cement particles leads to ITZ of smaller extent. This layer is highly heterogeneous and damaged and thus critical for the concrete behaviour [46]-[48]. According to

Königsberger et al. [48] two different types of failure exist for ITZs: ITZ-aggregate separation (related to delamination processes directly at the aggregate surface) and ITZ failure (related to cracking). An accurate understanding of the properties and behaviour of ITZ is one of the most important issues in the meso-scale analysis because damage is initiated at the weakest region and ITZ is just this weakest link in concrete. In our simulations, the ITZs were characterised by a weaker contact model between spheres (no additional particles forming ITZs were thus included). All spheres with the diameter larger than 1 mm were considered as aggregate (E_c=50 GPa, ν_c=0.2, μ=30^o, C=140 MPa, and T=25 MPa). All spheres with the diameter smaller than 1 mm were taken as the cement matrix (E_c=10 GPa, ν_c=0.2, μ=30^o, C=140 MPa and T=25 MPa). The large aggregate spheres with the diameter larger than 2 mm included ITZs only (due to their large perimeter) with the properties: E_c=5 GPa, ν_c=0.2, μ=30^o, C=100 MPa and T=15 MPa. Due to the information lack, the choice of the sphere diameter limit with respect to ITZs was arbitrary (our intention was to show a qualitative effect of ITZs on the concrete behaviour). The stiffness proportion between aggregate, cement matrix and ITZ was taken in the proportion 10:2:1 similarly as in the lattice beam model by Lilliu and van Mier [2].

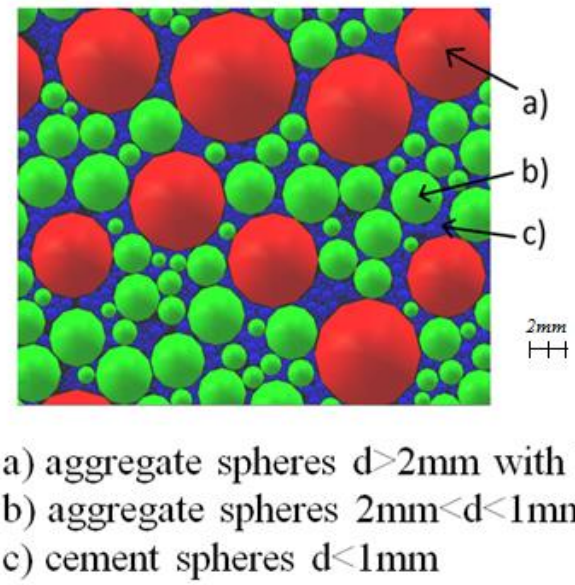

Figure 10: Structure of concrete as three-phase material (2D concrete specimen): a) aggregate spheres d>2 mm with ITZs, b) aggregate spheres 1 mm≤d≤2 mm and c) cement spheres d<1 mm

The 2D results of Fig.11 show that the presence of 3 phases improved the stress-strain curves in a post-peak regime by an increase of fracture energy. By including ITZs, a propagation way of cracks simply grew due to an increase of the material heterogeneity. An increase of the propagation length of ITZs diminished the strength but increased the ductility.

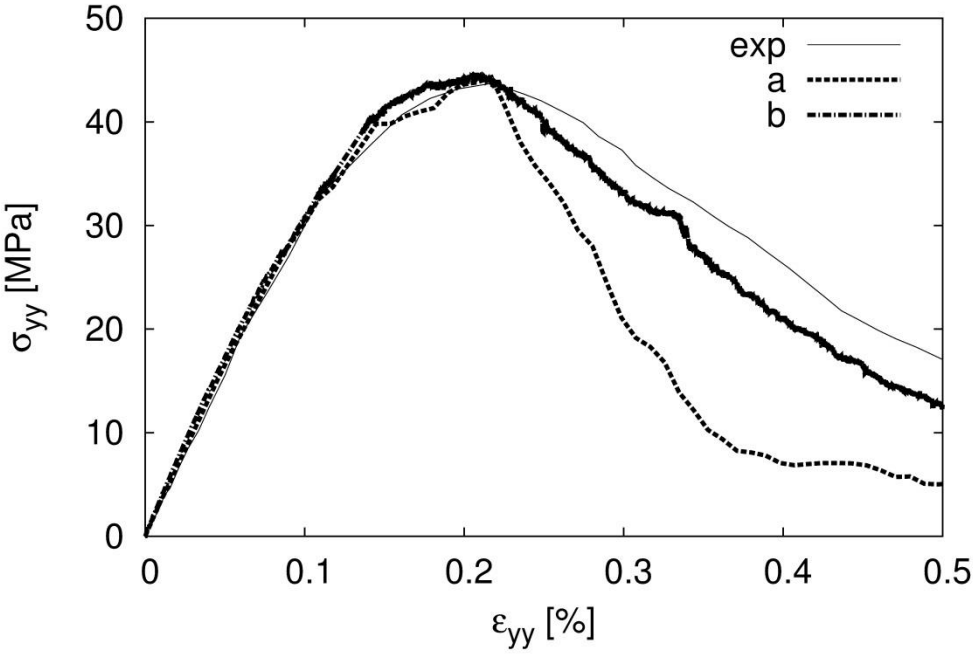

a) 1-phase material, b) 3-phase material

A)

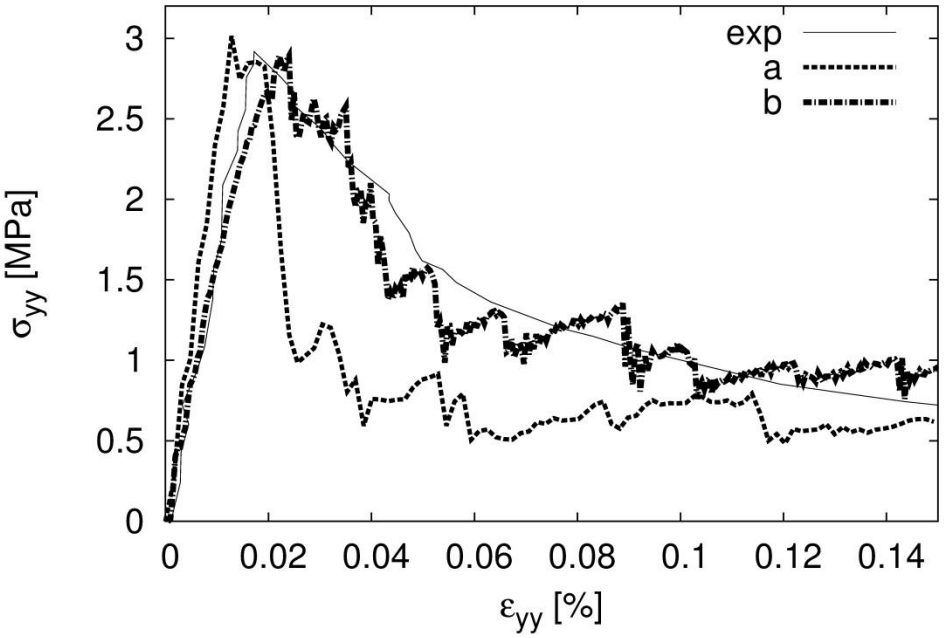

a) 1-phase material, b) 3-phase material

B)

Figure 11: Calculated stress-strain σ_y-ε_y curves during uniaxial compression (A) and uniaxial tension (B) from 2D DEM (d_{max}=12 mm, d_{min}=0.5 mm, d_{50}=2 mm and V_1=90%): a) 1-phase material, b) 3-phase material (ITZs at spheres with diameter larger than 2 mm), (exp – experiments by van Vliet and van Mier [41], [42])

Energy evolution

The evolution of the energy transformation with its elastic and dissipative characteristics and kinetic energy was demonstrated and played a fundamental role in the stability behaviour. The evolution of the total elastic energy was analysed during the continuing deformation process without separation into recoverable and stored terms. In a discrete concrete system there exist 3 main energies: elastic, kinetic and dissipated energy. In addition, the numerical dissipation also exists (Eq.6). The elastic internal energy stored at contacts N between aggregate grains E_e, expressed in terms of work of the elastic contact tangential forces F_s on the elastic tangential displacements U_s and the contact normal forces F_n on the elastic penetration depths U was

$$E_e = \sum_1^N \left(\frac{|F_s^e|^2}{2K_s}\right) + \frac{|F_n^e|^2}{2K_n}). \tag{6}$$

The kinetic energy E_c of grains was caused by their translation and rotation

$$E_c = \sum_1^N \left(\frac{1}{2} m v^2 + \frac{1}{2} I\, \dot{\omega}^2\right), \tag{7}$$

where m is the mass, I denotes the moment of inertia of a particle, v - translational velocity and $\dot{\omega}$ - rotational velocity.

The dissipated energy D_p, expressed in terms of work of the tangential (shear) forces on conjugate sliding displacements and moments on conjugate rotations was determined as:

$$D_p = D_p + \Delta D_p \qquad \text{with} \qquad \Delta D_p = \sum_1^N \left(F_s^{pl} U_s^{slip}\right) \tag{8}$$

Let us note that the dissipated energy was calculated incrementally at each time step and summed for the time period of contact of two respective spheres. In addition, the numerical dissipation D_n was specified during translation. The total accumulated energy

$$E = E_e + E_c + D_p + D_n \tag{9}$$

was equal to the external boundary work W expended on the assembly by the external vertical force on the vertical top displacement.

Figure 12 shows the calculated total accumulated energy E, elastic internally stored energy at contacts E_e, frictional dissipation D_p kinetic energy E_c and numerical damping D_n in the 2D concrete specimen during compression and tension. The internal accumulated energy E and external work W were almost equal during the tests. The total energy E in compression was almost 50 times higher than in tension. The evolution of the elastic internal energy in a normal and tangential direction was similar to the evolution of the mobilized specimen strength (expressed by the vertical normal stress along the top edge). The elastic internal energy E_e was obviously higher than the plastic damping D_p due to cohesion. The elastic energy portion due to tangential

force action was smaller (in particular for compression) than that due to the normal force action in view of the lack of plastic damping in a tangential direction.

Various kinds of energy had different proportions at different stress–strain stages. During compression the elastic internal energy E_e was equal to 60% at ε_y^p=0.15% (vertical normal strain corresponding to the maximum mobilized strength). The plastic dissipation D_p was equal to only 3% of the total energy at ε_y^p=0.15%. At ε_y=0.20%, it was already equal to 15% of the total energy. In turn, the numerical damping D_n equals 15% of the total energy at ε_y^p=0.15% and 70% of the total energy at ε_y^p=0.20%. In tension, the plastic dissipation D_p was negligible at ε_y^p=0.02%. At ε_y=0.20%, it was equal to 10% of the total energy. The elastic internal work E_e was equal to 40% at ε_y^p=0.02%. The numerical damping D_n equals 60% of the total energy at ε_y^p=0.15% and ε_y^p=0.20%. The plastic damping, kinetic energy and numerical damping start to significantly increase from the peak load at ε_y^p=0.15% (compression) and ε_y^p=0.02% (tension). The impact of the numerical damping was of a major importance although quasi-static problem was considered.

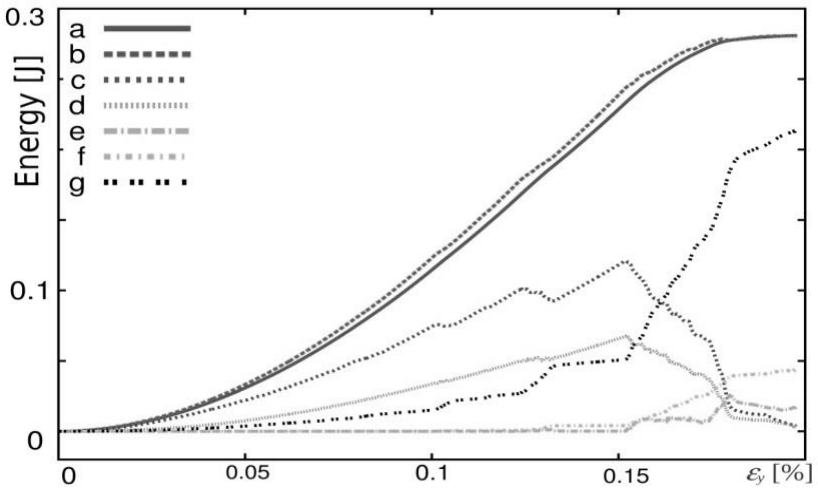

A)

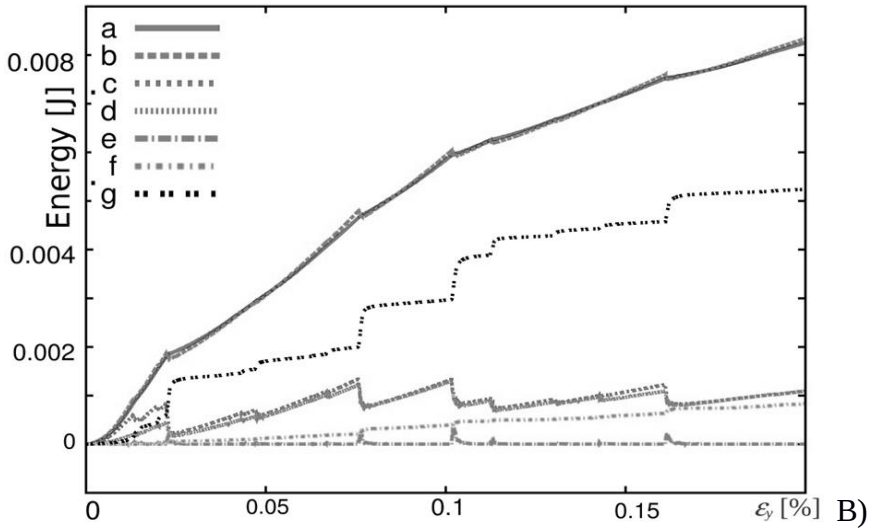

Figure 12: Calculated energies in 2D concrete specimens using DEM (1-phase material, d_{max}=12 mm, d_{min}=0.5 mm, d_{50}=2 mm and V_1=90%, α=0.08) during: A) uniaxial compression and B) uniaxial tension (α=0.1): a) external work, b) internal energy, c) normal elastic work in normal direction, d) elastic work in tangential direction, e) kinetic energy, f) plastic dissipated energy and g) numerical damping

4. Discrete results at micro-level

The macroscopic outcomes were mainly demonstrated for the one-phase concrete material. Figures 13 and 14 show the evolution of fracture in 2D concrete specimens (1-phase and 3-phase material) under compression and tension from two single runs. In the specimen subjected under compression, several inclined cracks occurred in the deformation direction (Fig.13A). In the specimen subjected to tension initially two almost horizontal cracks were initially created near the mid-height due to the assumed the deformation symmetry (Fig.13B). At failure, one crack dominated. In the 3-phase material, initially a lot of micro-cracks around grains (in ITZs) appeared (Figs.14A and 14B). Later, they connected with each other to form a main crack. The main crack was longer and more curved than in the 1-phase material. The coordination number and the total contact number continuously decreased in the specimens due to material dilatancy and successive fracture (Fig.15). At the beginning of the deformation, the total contact number in the specimen was approximately equal to 26’000 (compression) and 24’700 (tension) (Fig.15). When cracks were created, the contact number apparently decreased. At large deformation, the contact number was solely 22'500 (compression, ε_y=0.3%) and 23'000 (tension, ε_y=0.05%).

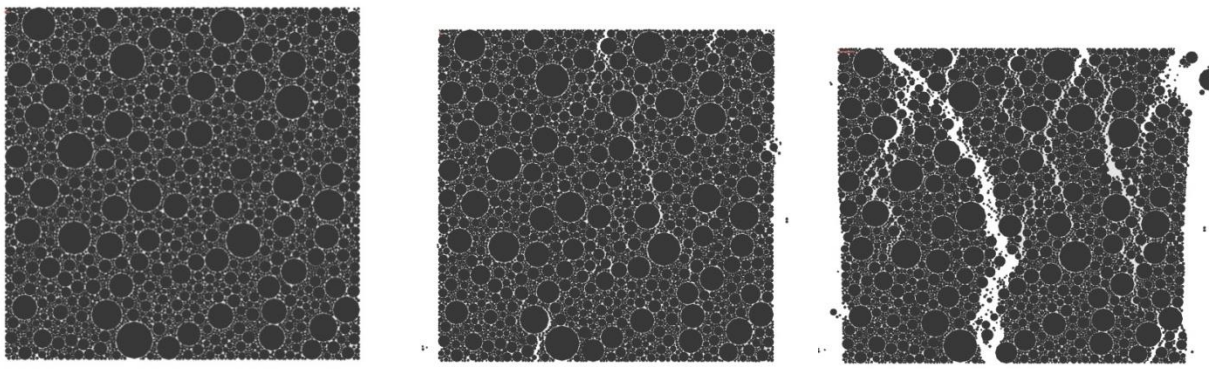

a) b) c)

A)

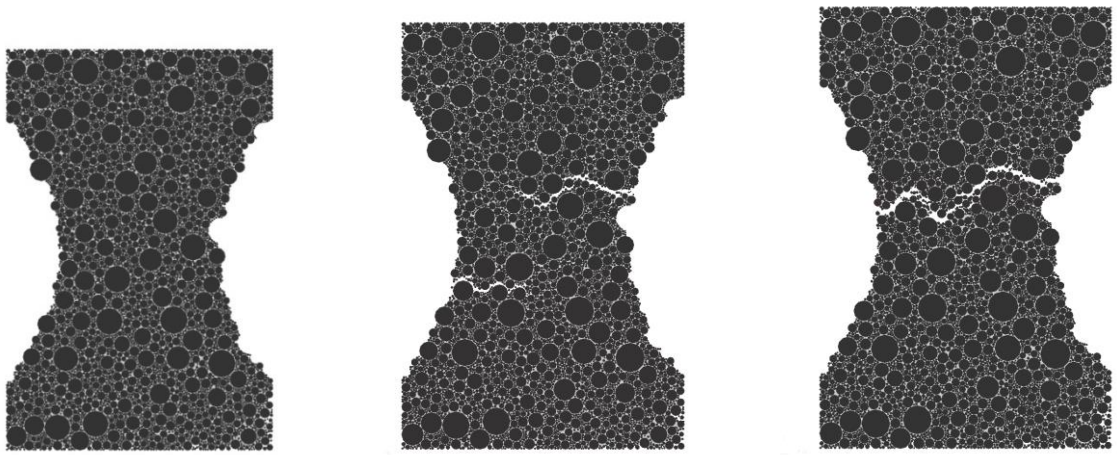

a) b) c)

B)

Figure 13: Fracture evolution in concrete specimen using 2D DEM (one-phase material, (d_{max}=12 mm, d_{min}=0.5 mm, d_{50}=2 mm and V_1=90%): A) during uniaxial compression (a) ε_{yy}=0.05% (initially), b) ε_{yy}=0.15% (peak), c) ε_{yy}=0.25% (after peak) and B) during uniaxial tension (ε_{yy}=0.005% (initially), b) ε_{yy}=0.015% (peak), c) ε_{yy}=0.05%))

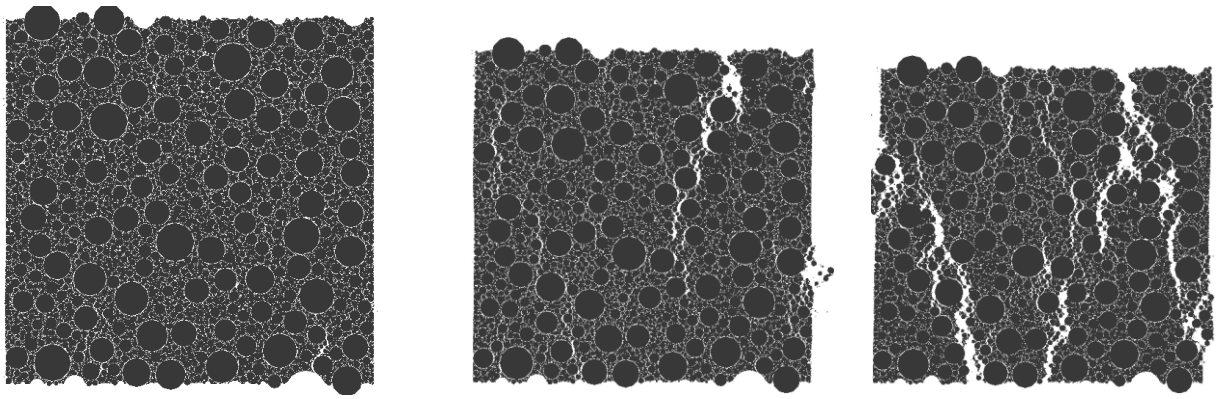

a) b) c)

A)

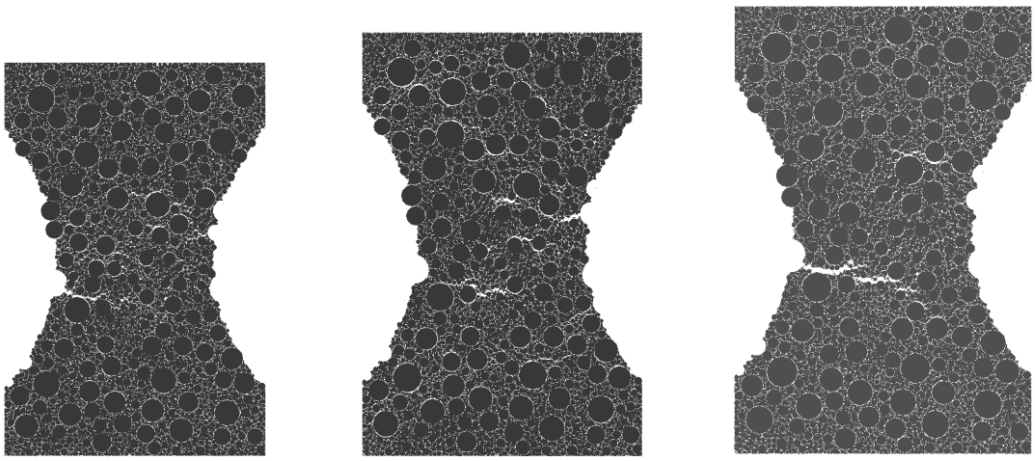

a) b) c)

B)

Figure 14: Fracture evolution in concrete specimen using 2D DEM (three-phase material, (d_{max}=12 mm, d_{min}=0.5 mm, d_{50}=2 mm and V_1=90%): A) during uniaxial compression (a) ε_y=0.05% (initially), b) ε_y=0.15% (peak), c) ε_y=0.25% (after peak) and B) during uniaxial tension (ε_y=0.005% (initially), b) ε_y=0.015% (peak), c) ε_y=0.05%))

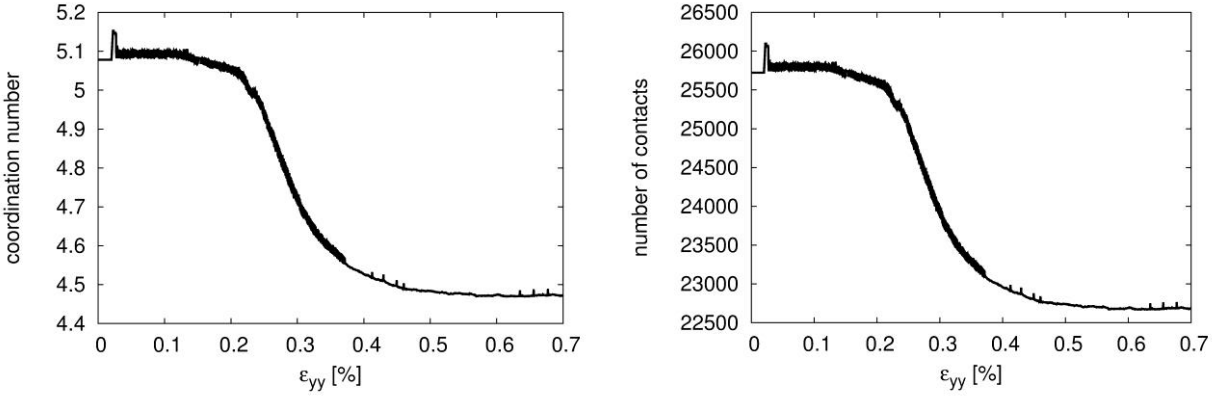

a) b)

A)

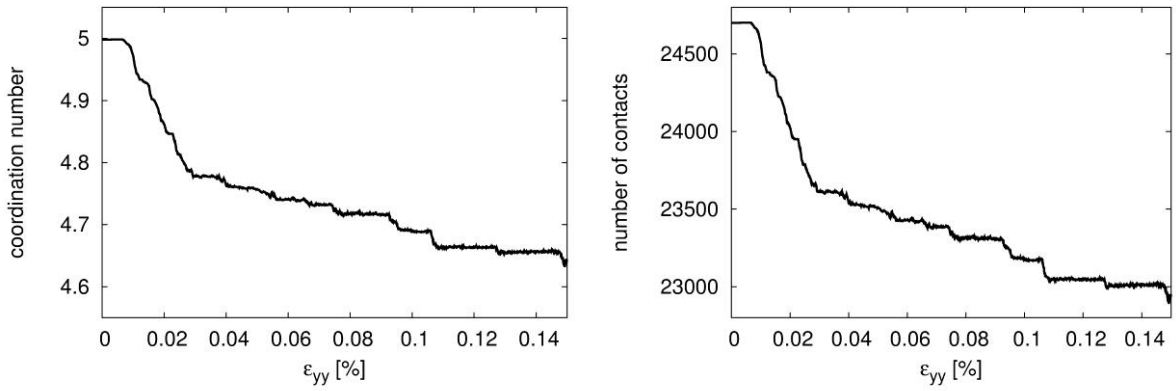

a) b)

B)

Figure 15: Evolution of coordination number (a) and contact number (b) in 2D concrete specimens from DEM (1-phase material, d_{max}=12 mm, d_{min}=0.5 mm, d_{50}=2 mm and V_1=90%): A) uniaxial compression and B) uniaxial tension

Figures 16-19 demonstrate the distribution of changes of void ratio e-e_o (where e_o is initial void ratio), resultant sphere rotations and displacement fluctuations during deformation of 2D specimens. Changes of void ratio were calculated from the quadratic cell equal to $5d_{50}\times5d_{50}$ moved by d_{50}. The plots of displacement fluctuations were obtained by drawing the displacement difference vector ($\vec{V_i} - \vec{V}_{avg}$) for each sphere with respect to the background translation corresponding to the homogeneous (affine) strain in the entire specimen ($\vec{V_i}$ represents the sphere displacements during k=1000 iterations (with the time increment $\Delta t_s = 10^{-8} s$) and $\vec{V}_{avg} = \frac{1}{n}\sum_i^n \vec{V}_i$ is the average displacement in the entire specimen).

The porosity distribution was non-uniform in the concrete specimens (Fig.16). Localized porosity regions were subjected to a local volume increase. In these regions, some small sphere rotations appeared when the contacts were broken (in the order of about 1^o for compression and 0.01^o for tension) (Figs.17 and 18). The spheres might continuously rotate (tension) or after an initial significant increase they stabilized (compression), Fig.18.

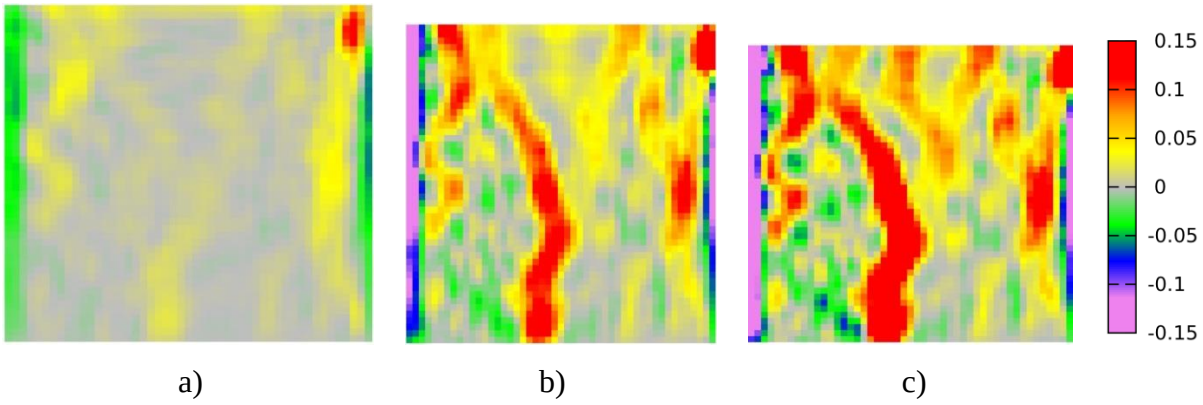

a) b) c)

A)

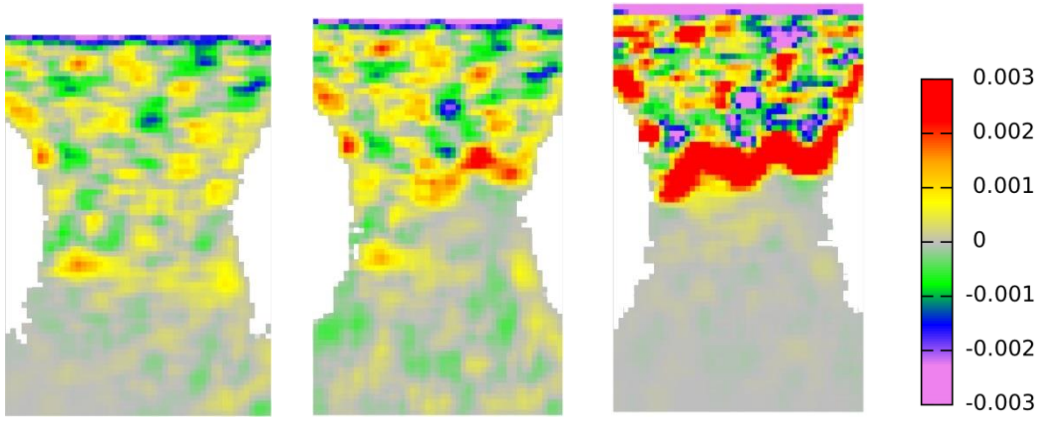

a) b) c)

B)

Figure 16: Calculated distribution of local void ratio changes (red colour – volume increase, pink colour – volume decrease) in 2D concrete specimens using DEM (1-phase material, d_{max}=12 mm, d_{min}=0.5 mm, d_{50}=2 mm and V_1=90%) during: A) uniaxial compression at ε_y=0.15% (a), ε_y=0.20% (b) and ε_y=0.25% (c) and B) uniaxial tension at ε_y=0.010% (a), ε_y=0.015% (b) and ε_y=0.050% (c) (sign (+) - dilatancy)

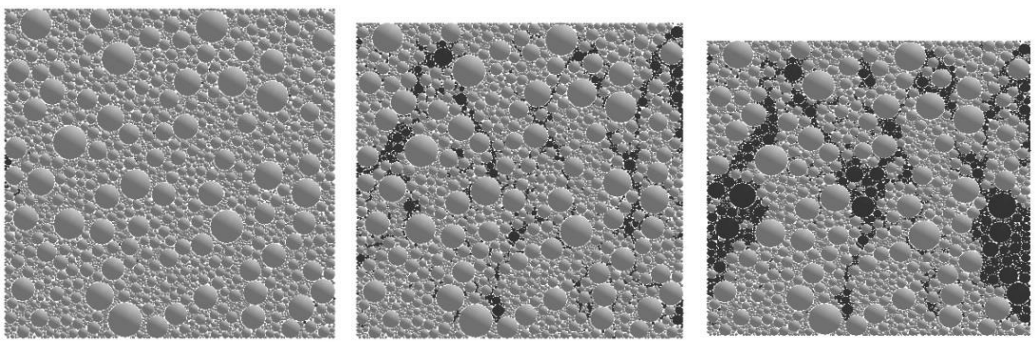

A)

a) b) c)

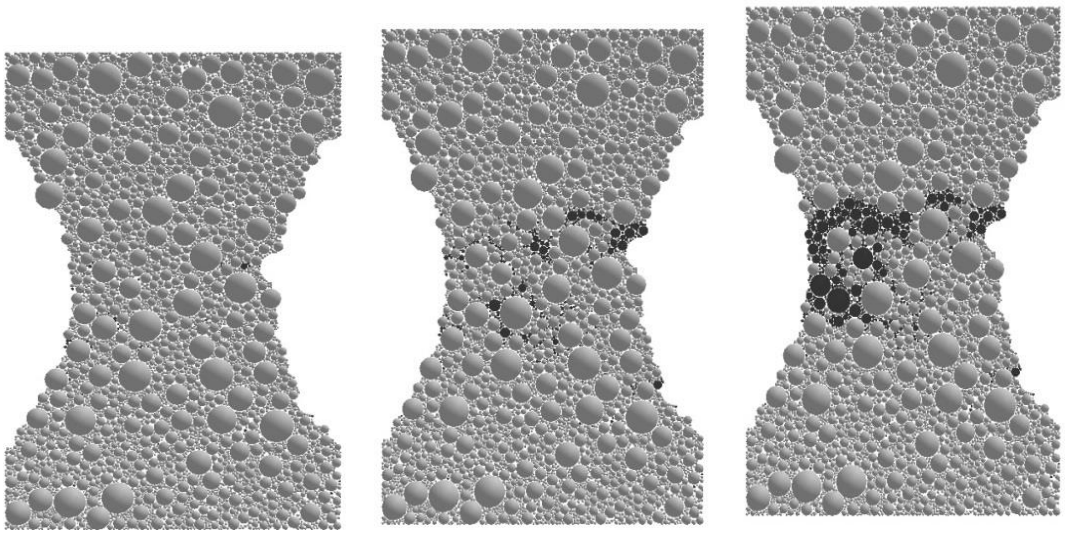

B)

a) b) c)

Figure 17: Calculated distribution of resultant sphere rotations in 2D concrete specimens using DEM (1-phase material, d_{max}=12 mm, d_{min}=0.5 mm, d_{50}=2 mm and V_1=90%) during: A) uniaxial compression at ε_y=0.15% (a), ε_y=0.20% (b) and ε_y=0.25% (c) and B) uniaxial tension at ε_y=0.01% (a), ε_y=0.015% (b) and ε_y=0.05% (c) (black colour - higher rotations)

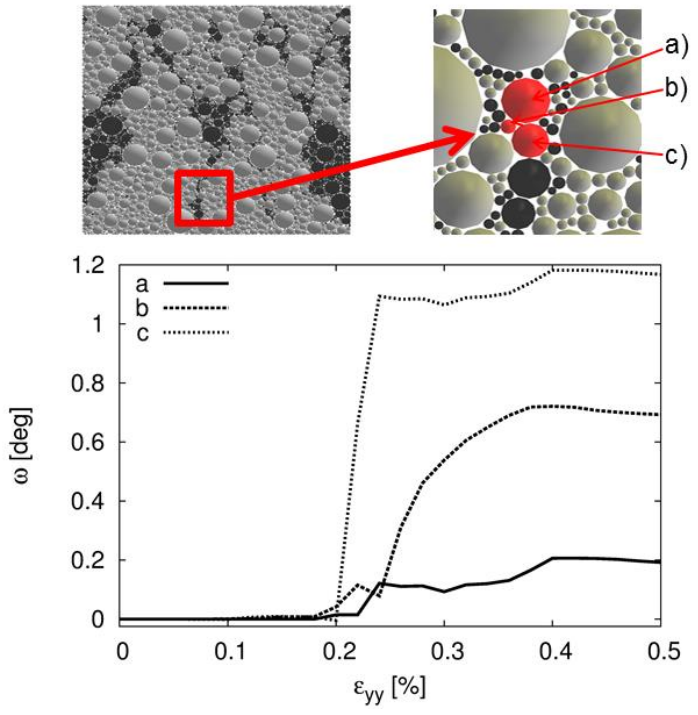

A)

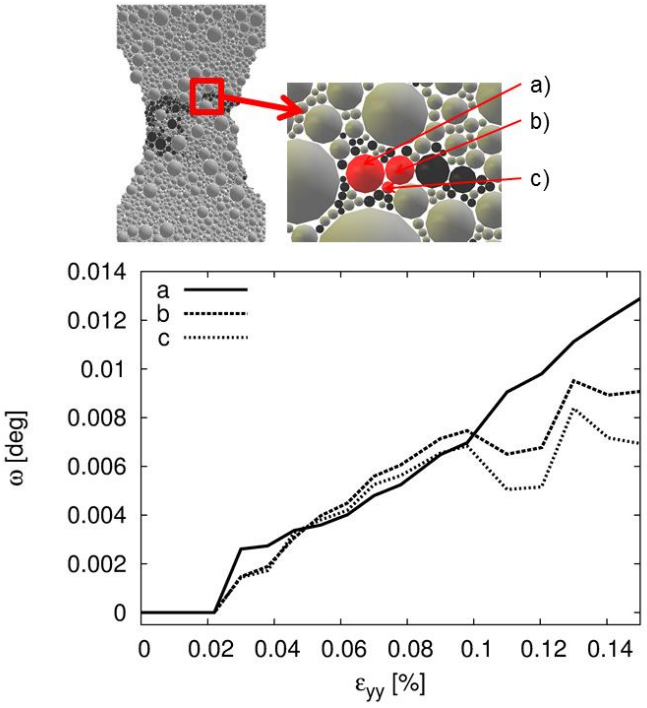

B)

Figure 18: Calculated evolution of sphere rotations in 2D concrete specimens using DEM (1-phase material, d_{max}=12 mm, d_{min}=0.5 mm, d_{50}=2 mm and V_1=90%) during: A) uniaxial compression and B) uniaxial tension (considered are 3 different spheres 'a', 'b' and 'c')

Figure 19 presents spontaneous displacement fluctuations having the form of cells circulating as quasi-rigid bodies (so-called vortex structures) which were the inherent characteristics of shear localization in granular materials [34], [49], [50]. The individual sphere displacements were able to form long-range deformation vortex structures which rotated as rigid bodies. During compression and tension one vortex was obtained which was more visible during tension (Figs.19a and 19b). Its diameter was 1 cm ($5\times d_{50}$) for tension and 0.6 cm ($3\times d_{50}$) for compression. It started to form before the peak on the stress-strain curve and disappeared when a macro-crack was created (Figs.19d and 19e). Its rotation was about 0.1-0.4^o. The vortex structure was well visible if the number of iterations k was high enough, e.g. $k\geq1000$ ($\Delta t_s = 10^{-8}$). It is difficult to say at this stage of research whether vortex structures have any significant impact on the concrete behaviour and how they could be taken into account in strength calculations. The reason is that the mechanisms ruling the creation of vortices are not fully recognized yet.

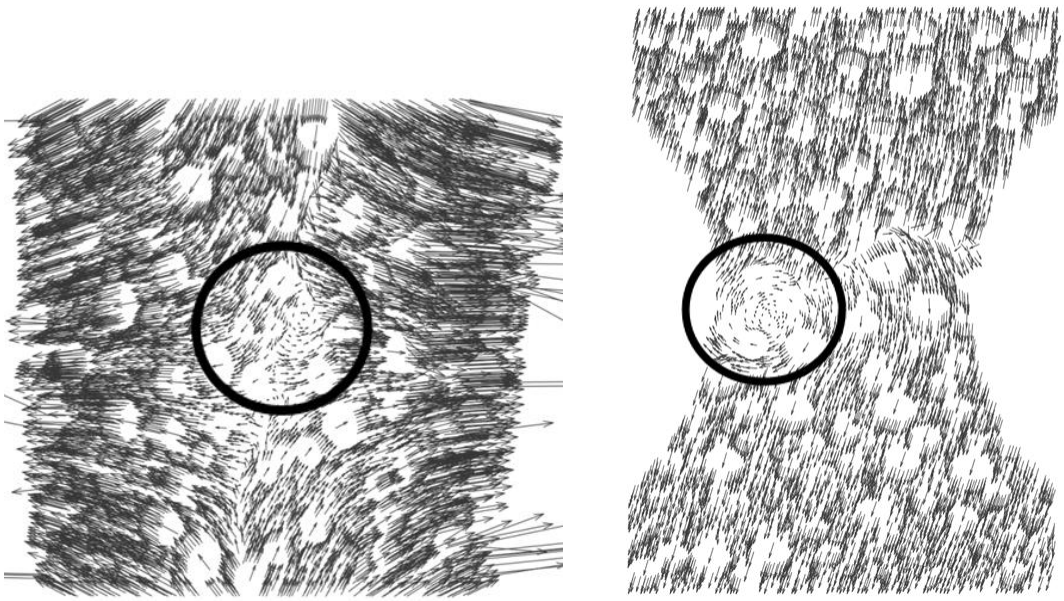

a) b)

c)

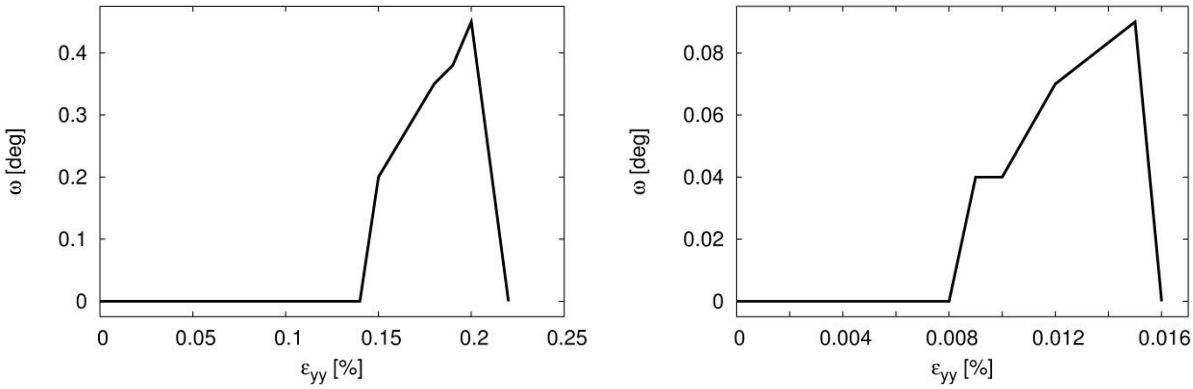

d) e)

Figure 19: Calculated displacement fluctuations in 2D concrete specimens using DEM (1-phase material, d_{max}=12 mm, d_{min}=0.5 mm, d_{50}=2 mm and V_1=90%): a), b) distribution during uniaxial compression at ε_y=0.15% (a) and uniaxial tension at ε_y=0.02% (b), c) zoom on vortex in uniaxial tension, d), e) vortex rotation evolution versus vertical normal strain during uniaxial compression (d) and uniaxial tension (e)

The evolution of the contact force network in the concrete specimens was demonstrated in Fig.20. Forces were transmitted via two-phase network of contact forces: a strong contact force network (so-called force chains), which bear the majority of the loading and transmit it on the entire system and were the predominant structure of internal forces at micro-scale, and a complementary surrounding weak network of particles that provides lateral stability to force chains. The thickness of lines in Fig.20 represents the magnitude of normal contact force between two particles (red colour –normal compressive contact forces and blue colour – normal tensile contact forces). The maximum single sphere contact force was about: 200 N (compression) and 45 N (tension). The distribution of internal contact forces was non-uniform (Fig.20). During compression, the high normal compressive forces were in a direction parallel to the deformation direction and small normal tensile forces were horizontally directed. In uniaxial tension, high normal tensile forces were parallel to the deformation direction. However, in a fractured region during tension, some compressive forces also surprisingly occurred. The number of contacts diminished in localized zones due to cracking connected to dilatancy (Fig.15), leading to a reduction of the amount of force chains. Initially all chain forces grew during loading (Fig.21). If a single force chain broke due to cracking, the neighbouring force chains took on the load up to their own breakage (Fig.21).A relationship between collapse of force chains, local porosity changes and appearance of vortices merits further investigations.

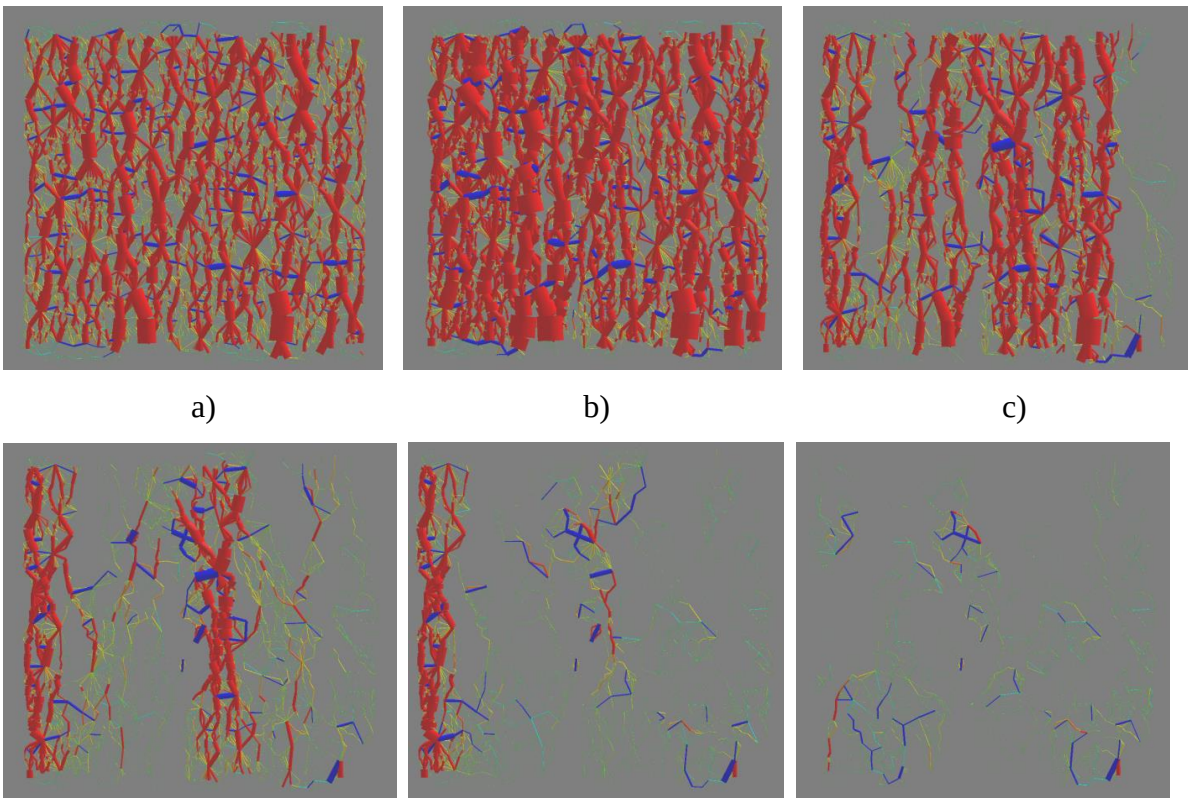

a) b) c)

d) e) f)

A)

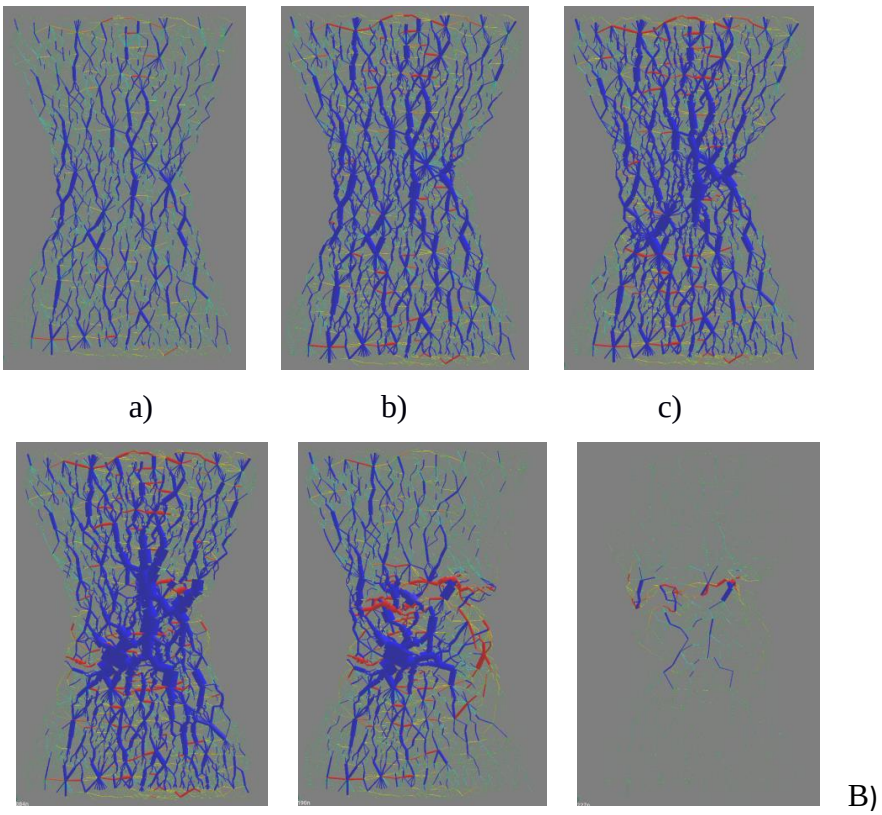

Figure 20: Calculated distribution of contact forces in 2D concrete specimens using DEM (1-phase material, d_{max}=12 mm, d_{min}=0.5 mm, d_{50}=2 mm and V_1=90%) during deformation: A) uniaxial compression at ε_y=0.10% (a), ε_y=0.18% (b), ε_y=0.21% (c) ε_y=0.23% (d), ε_y=0.25% (e) and ε_y=0.3% (f) and B) uniaxial tension at ε_y=0.005% (a), ε_y=0.008% (b), ε_y=0.010% (c) ε_y=0.017% (d), ε_y=0.025% (e) and ε_y=0.03% (f) (red colour –normal compressive contact forces and blue colour – normal tensile contact forces)

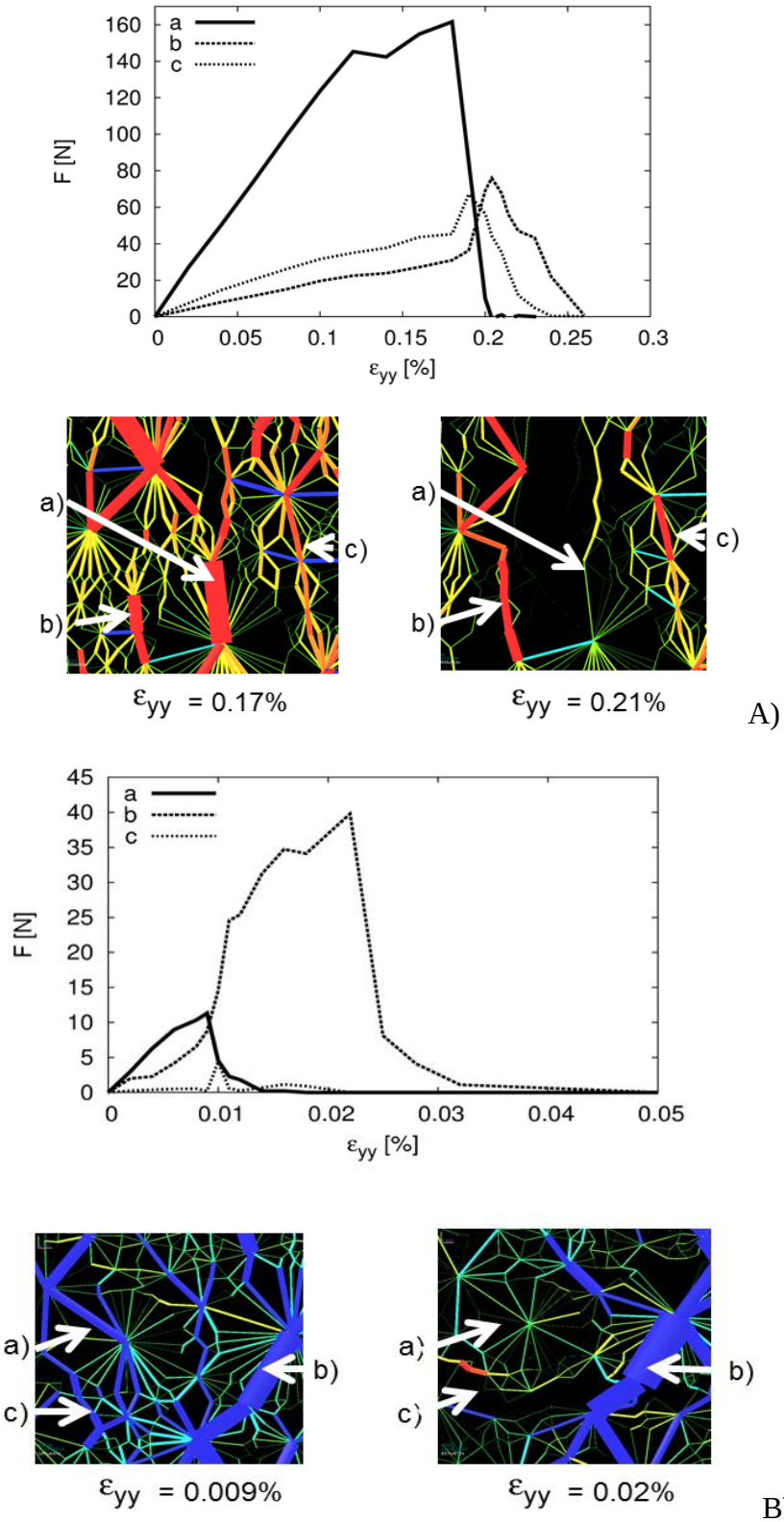

Figure 21: Calculated evolution of forces in neighbouring chains ('a', 'b' and 'c') in concrete specimens during deformation using DEM (1-phase material, d_{max}=12 mm, d_{min}=0.5 mm, d_{50}=2 mm and V_1=90%): A) uniaxial compression and B) uniaxial tension (red colour – normal compressive contact forces and blue colour – normal tensile contact forces)

The calculated resultant sphere displacements from the quadratic cell equal to $5d_{50}\times5d_{50}$ moved by d_{50} across a localized zone during compression and tension were depicted in Fig.22. In order

to calculate more accurately the width of a localized zone, the calculated sphere displacements were fitted first by the error function ERR [51]

$$ERF(x) = \frac{2}{\sqrt{\pi}} \int_0^x e^{-t^2}\, dt. \tag{10}$$

The halved error function evaluated at $\frac{x}{s\sqrt{2}}$ for positive *x*-values gives the probability that a measurement under the influence of normally distributed errors with the standard deviation *s* has a distance less than *x* from the mean value. The fitting function parameter *s* in Eqs.10 was used to determine the width of a localized zone w_c (based on the experimental results [47], the width w_c might be calculated from the equation $w_c=4\times s$). Thus, 95% of the values of the normal distribution function area were within the distance of 2 standard deviations in both directions from the mean value. The calculated width of a localized zone changes between 1.5-3.0 mm during compression and between 1.5-2.5 mm during tension based on the displacement jump shown in Fig.22 [i.e. $(0.125\text{-}0.25)\times d_{max}$ and $(0.75\text{-}1.5)\times d_{50}$]. It was approximately in agreement with experimental results by Skarzynski and Tejchman [52] for usual sand and gravel concrete notched beams under 3-point bending obtained by means of the digital image correlation technique DIC technique: 2.5-3.5 mm. It was approximately equal to the width of a damage zone at the same place (3-5 mm) which corresponded to a region with broken contacts between spheres (Fig.23).

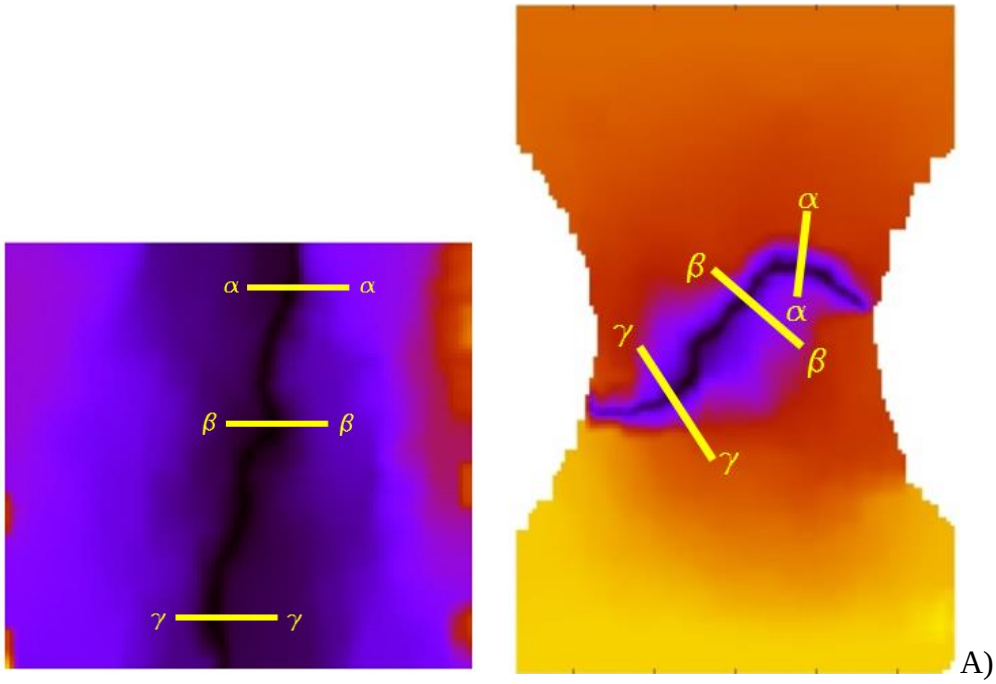

A)

I) II)

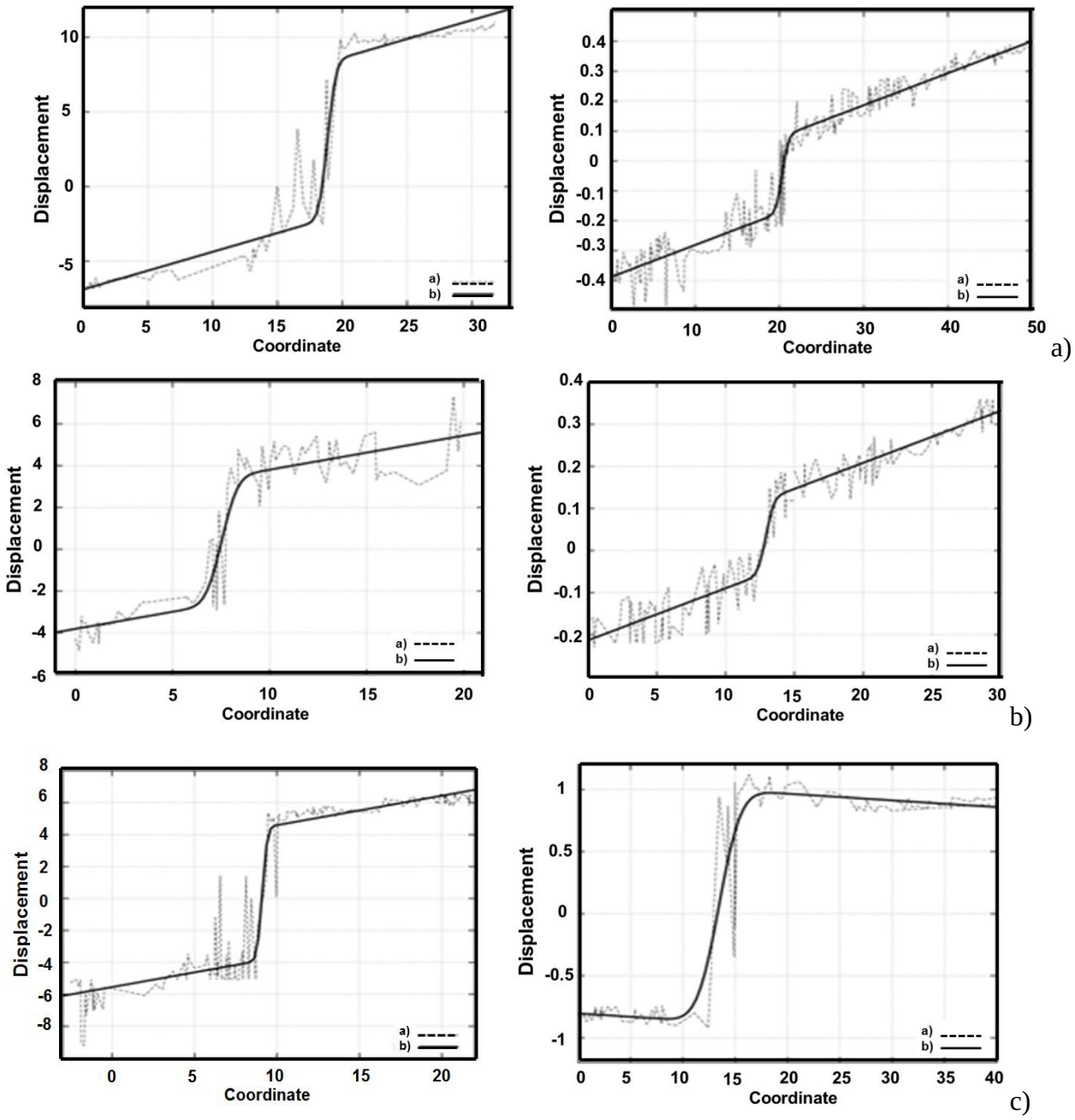

Figure 22: Calculated displacements along 2D specimen height during uniaxial compression at ε_{yy}=0.2% (I) and uniaxial tension at ε_{yy}=0.02% (II) versus section coordinate across localized zone in 2D concrete specimens using DEM: A) displacement map with marked sections across localized zone, a) displacement profile along line α-α, b) displacement profile along β-β, c) displacement profile along profile γ-γ (dashed line correspond to DEM result and solid line correspond to error function ERR)

Summing up, the numerical simulations of uniaxial compression and uniaxial tension tests show that discrete model was capable to satisfactorily reproduce the most important macroscopic properties of cohesive-frictional materials in uniaxial load states without it being necessary to

describe perfectly the concrete micro-structure with respect to the aggregate shape, aggregate distribution curve, minimum aggregate size and ITZs' width. The main advantage of the described model is that the micro-structure of the real concrete can be simulated and its effect on the concrete behaviour may be evaluated in numbers using simple contact laws. In addition, different micro-structural events (strictly connected to each others) may be studied in detail. The discrete simulation outcomes should contribute to a better calibration of enhanced constitutive models for concrete with respect to non-local and second-gradient terms that requires an accurate description of the micro-scale deformation within localized zones and a characteristic length of micro-structure [3], [6]. The results will also contribute to a better calibration of our discontinuous constitutive FE models and a transition point in our combined continuous-discontinuous FE models [3], [53], [54]. In turn, the knowledge on porosity-force chain correlations will allow for introducing stress fluctuations (connected to a collapse of force chains) to capture the stress-strain evolution more realistically.

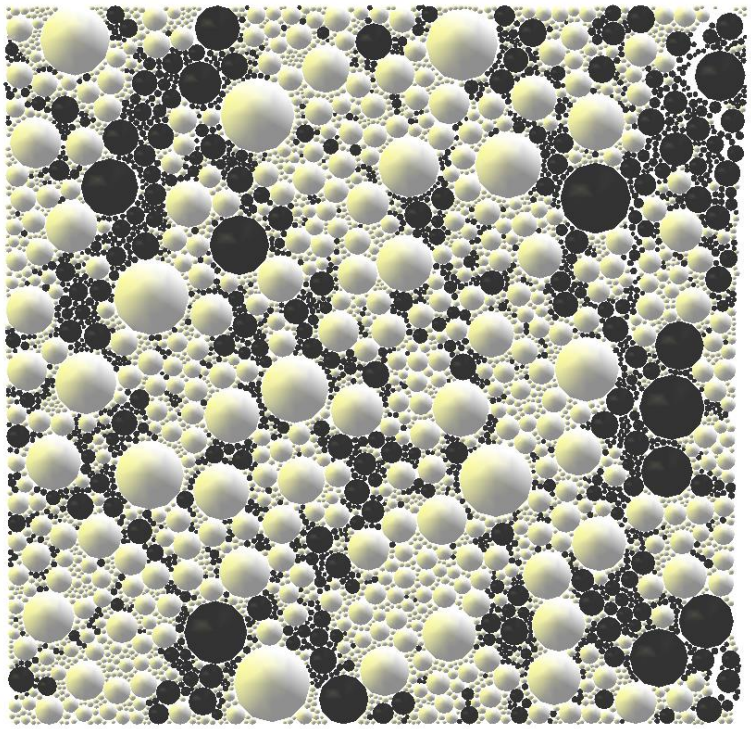

a)

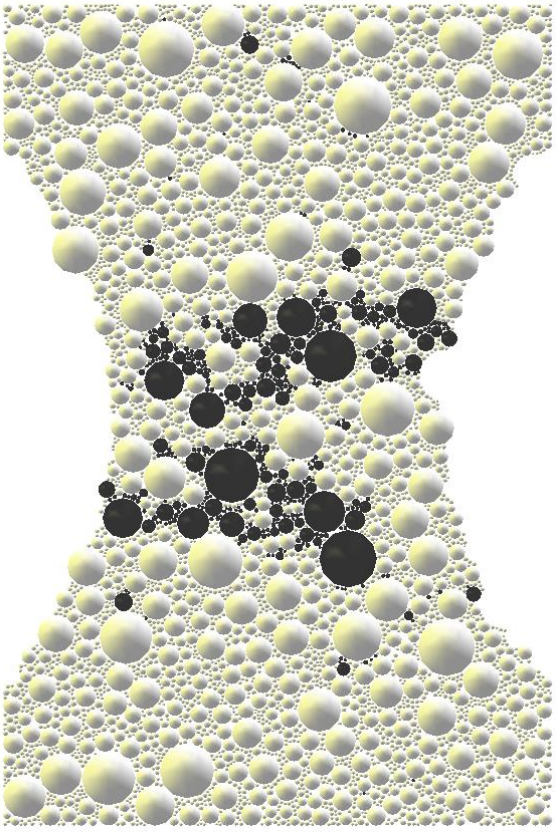

b)

Figure 23: Calculated regions of damaged contacts between grains in 2D specimen during: a) uniaxial compression at ε_{yy}=0.2% and b) uniaxial tension at ε_{yy}=0.02% (black spheres correspond to spheres with broken contacts)

The limitations of our model is the long computation time and the knowledge lack on the mechanical and geometric properties of micro-structure components (e.g. of ITZs). Moreover, in order to describe the concrete behaviour under high confining pressure, aggregate crushing and more sophisticated contact models will be probably required [43], [44].

In the next step, the 3D fracture process will be investigated using DEM in experimental notched concrete beams wherein DIC was used to measure the width of a localized zone [52]. When constructing the concrete beams, the real internal concrete 3D structure used in tests will be reproduced.

6. Summary and conclusions

Comparing the numerical simulations with the experimental tests shows that our simple discrete model was able to realistically reproduce the experimental results for real concrete at macro-level under quasi-static uniaxial compression and tension and to describe some influential micro-

structural phenomena occurring at particle level which strongly affect the macroscopic behaviour.

DEM proved its capability to model concrete. The agreement of discrete stress-strain results with experimental ones increased with 3D analyses, presence of small particles and 3 different phases (aggregate, cement matrix, ITZs). The denser the specimen, the higher was the concrete strength and smaller is the material ductility. The smaller the minimum sphere size, the larger was the concrete tensile strength and compression ductility. The tensile strength increased with decreasing specimen size. Since the discrete results strongly depended on the internal concrete micro-structure, it is advantageous to reproduce it realistically in 3D calculations (the 3D results strongly differed from the 2D simulation results).

The distribution of internal contact forces in concrete specimens was non-uniform. The number of contact forces continuously decreased in concrete specimens due to dilatancy connected to material fracture. Some grain rotations occurred in fractured regions (in the order of 1^o for compression and 0.01^o for tension). Vortex structures might also form in localized regions. The width of a 2D localized zone based on grain displacement varied between 1.5-3 mm. It was similar to the width of a damage zone characterized by the breakage of spherical contacts.

The plastic dissipation was smaller than the internal elastic energy due to cohesion. The plastic dissipation and kinetic energy significantly increased after the peak load during a cracking process.

Acknowledgments

Research work has been carried out within the project: "*Innovative ways and effective methods of safety improvement and durability of buildings and transport infrastructure in the sustainable development*" financed by the European Union (POIG.01.01.02-10-106/09-01) and "*Experimental and theoretical investigations of micro-structural phenomena inside of shear localization in granular materials*" financed by Polish National Research Centre (grant 2011/03/B/ST8/05865).

References

[1] Bažant, Z. and Planas, J. Fracture and size effect in concrete and other quasi-brittle materials. *CRC Press LLC, Boca Raton* (1997).

[2] Lilliu, G. and van Mier, J.G.M. 3D lattice type fracture model for concrete. *Engineering Fracture Mechanics* 70, 927-941 (2003).

[3] Tejchman J. and Bobiński J. Continuous and discontinuous modelling of fracture in concrete using FEM. *Springer, Berlin-Heidelberg* (eds. W. Wu and R. I. Borja) (2013).

[4] Pijaudier-Cabot, G. and Bažant, Z.P. Nonlocal damage theory. *Journal of Engineering Mechanics* ASCE 113(10), 1512-1533 (1987).

[5] Gitman, I. M., Askes, H. and Sluys, L.J. Coupled-volume multi-scale modelling of quasi-brittle material. *European Journal of Mechanics A/Solids* 27, 302-327 (2008).

[6] Skarzynski, Ł. and Tejchman, J. Calculations of fracture process zones on meso-scale in notched concrete beams subjected to three-point bending. *European Journal of Mechanics A/Solids* 29 (4), 746-760 (2010).

[7] Kim, S.M. and Abu Al-Rub, R. K. Meso-scale computational modeling of the plastic-damage response of cementitious composites. *Cement and Concrete Research* 41, 339-358 (2011).

[8] Shahbeyk, S., Hosseini, M. and Yaghoobi, M.: Mesoscale finite element prediction of concrete failure. *Computational Materials Science* 50 (7), 1973-1990 (2011).

[9] Hentz, S., Daudeville, L. and Donze, F. Identification and validation of a Discrete Element Model for concrete. *Journal of Engineering Mechanics ASCE* 130 (6), 709-719 (2004).

[10] Kozicki, J. and Tejchman, J. Modelling of fracture processes in concrete using a novel lattice model. *Granular Matter* 10, 377-388 (2008).

[11] Sakaguchi, H. and Mühlhaus, H.-B. Mesh free modelling of failure and localization in brittle materials. *Deformation and Progressive Failure in Geomechanics* (eds.: A. Asaoka, T. Adachi and F. Oka), 15-21 (1997).

[12] Donze, F.V., Magnier, S.A., Daudeville, L. and Mariotti, C. Numerical study of compressive behaviour of concrete at high strain rates. *Journal for Engineering Mechanics,* 122(80), 1154-1163 (1999).

[13] D'Addetta, G.A., Kun, F. and Ramm, E. On the application of a discrete model to the fracture process of cohesive granular materials. *Granular Matter* 4, 77-90 (2002).

[14] Potyondy, D.O. and Cundall, P. A. A bonded-particle model for rock. *Int. J. Rock Mechanics and Mining Sciences* . 41(8), 1329-1364 (2004).

[15] Dupray, F., Malecot, Y., Daudeville, L. and Buzaud, E. A mesoscopic model for the behaviour of concrete under high confinement. *International Journal for Numerical and Analytical Methods in Geomechanics* 33, 1407-1423 (2009).

[16] Rojek, J., Oñate, E., Labra, C. and Kargl, H. Discrete element simulation of rock cutting. *Int. J. Rock Mechanics and Mining Sciences* 48, 996-1010 (2011).

[17] Obermayr, M., Dressler, K., Vrettos, C. and Eberhard, P. A bonded-particle model for cemented sand. *Computers and Geotechnics* 49, 299-313 (2013).

[18] Carol, I., López, C.M. and Roa, O. Micromechanical analysis of quasi-brittle materials using fracture-based interface elements. *Int J Numerical Methods in Engineering* 52,193-215, 2001.

[19] Caballero, A., Carol, I. and López C.M. New results in 3D meso-mechanical analysis of concrete specimens using interface elements, *Computational Modelling of Concrete Structures, EURO-C (eds.:G. Meschke, R. de Borst, H. Mang and N. Bićanić), Taylor and Francis Group*, 43, 52, (2006).

[20] Kawai, T. New discrete models and their application to seismic response analysis of structure. *Nuclear Engineering and Design* 48, 207-229 (1978).

[21] Herrmann, H. J., Hansen, A. and Roux, S. Fracture of disordered, elastic lattices in two dimensions. *Physical Rev. B*, 39, 637-647 (1989).

[22] Vervuurt, A., van Mier, J.G.M. and Schlangen, E. Lattice model for analyzing steel-concrete interactions. *Computer Methods and Advances in Geomechanics* (eds.: Siriwardane and Zaman), Balkema, Rotterdam 713-718, 1994.

[23] Jirásek, M. and Bažant Z. P. Particle model for quasi-brittle fracture and application to sea ice. *J. Eng. Mech.* 121(9), 1016-1025 (1995).

[24] Schlangen, E. and Garboczi, E. J. Fracture simulations of concrete using lattice models: computational aspects. *Engineering Fracture Mechanics* 57, 319-332 (1997).

[25] Cusatis, G., Bažant, Z.P. and Cedolin, L. Confinement-shear lattice model for concrete damage in tension and compression: I. theory. *ASCE Journal of Engineering Mechanics* 129, 12, 1439-1448 (2003).

[26] Bolander, J.E. and Sukumar, N. Irregular lattice model for quasi-static crack propagation. *Phys Rev B* 71, 094106 (2005).

[27] Yip, M., Li, Z., Liao, B.-S. and Bolander, J.E. Irregular lattice models of fracture of multiphase particulate materials. *Int. J. Fract*. 140, 113–124 (2006).

[28] Kozicki, J. and Tejchman, J. Effect of aggregate structure on fracture process in concrete using 2D lattice model. *Archives of Mechanics* 59, 4-5, 1-20 (2007).

[29] Grassl, P. and Jirásek, M. Meso-mechanically motivated nonlocal models for modelling of the fracture process zone in quasi-brittle materials. *Proc. 8th.World Congress on Computational Mechanics (WCCM8)*, 1-2 (2008).

[30] Kozicki, J., Tejchman, J. and Mróz, Z. Effect of grain roughness on strength, volume changes, elastic and dissipated energies during quasi-static homogeneous triaxial compression using DEM. *Granular Matter* 14, 4, 457-468 (2012).

[31] Kozicki, J. and Donze, F. A new open-source software developer for numerical simulations using discrete modeling methods. *Computer Methods in Applied Mechanics and Engineering*, 197, 4429-4443 (2008).

[32] Šmilauer, V. and Chareyre, B.: Yade DEM Formulation. *Manual* (2011).

[33] Widulinski, L., Tejchman, J., Kozicki, J. and Leśniewska, D.: Discrete simulations of shear zone patterning in sand in earth pressure problems of a retaining wall. *Int. J. Solids and Structures* 48, 7-8, 1191-1209 (2011).

[34] Kozicki, J., Niedostatkiewicz, M., Tejchman, J. and Mühlhaus, H.-B. Discrete modelling results of a direct shear test for granular materials versus FE results. *Granular Matter* 15, 5, 607-627 (2013).

[35] Nitka, M., Tejchman, J., Kozicki, J. and Leśniewska, D. DEM analysis of micro-structural events within granular shear zones under passive earth pressure conditions. *Granular Matter* (2014) (under review).

[36] Kruggel-Emden, H., Simsek, E., Rickelt, S., Wirtz, S. and Scherer, V. Review and extension of normal force models for the Discrete Element Method. *Powder Technol*. 171 (3), 157-173 (2007).

[37] Ergenzinger, Ch., Seifried, R. and Eberhard, P. A discrete element model to describe failure of strong rock in uniaxial compression. *Granular Matter* 13, 341-364 (2011).

[38] Šmilauer, V. Cohesive Particle Model using the Discrete Element Method on Yade Platform. *PhD Thesis Czech Technical University in Prague and University of Grenoble* (2010).

[39] Tapias, M.A., Alonso, E.E. and Gili, J.A.: Analysis of micro-properties for triaxial behaviour on coarse aggregates using DEM. *II International Conference on Particle-based Methods-Fundamentals and Applications PARTICLES 2011 E. Oñate and D.R.J. Owen (eds)* (2011).

[40] Cundall, P. A. and Hart, R.: Numerical modelling of discontinua. *J. Eng. Comp*. 9(2), 101-113 (1992).

[41] van Mier, J.G.M.: Multiaxial strain-softening of concrete. Part I: Fracture. *Materiaux et Constructions* 19, 111 (1986).

[42] van Vliet, M.R.A. and van Mier, J.G.M. Experimental investigation of size effect in concrete and sandstone under uniaxial tension. *Engineering Fracture Mechanics* 65, 165-188 (2000).

[43] Tran, V.T., Donze, F.V. and Marin, P. Discrete element model of concrete under high confining pressure. *Fracture Mechanics of Concrete and Concrete Structures, Recent Advances in Fracture Mechanics of Concrete, B.H. Oh, et al. (eds)*, Seoul, Korea (2010).

[44] Daudeville, L. and Malecot, Y. Concrete structures under impact. *European Journal of Environmental and Civil Engineering* 15, 101-140 (2011).

[45] Agnolln, I. and Roux, J.-N. Internal states of model isotropic granular packings. I. Assembling process, geometry, and contact networks. *Physical Review* E 76, 061302 (2007).

[49] Kuhn, M.R. Structured deformation in granular materials. *Mechanics of Materials* 31(6), 407-429 (1999).

[46] Scrivener, K.L., Crumbie, A.K. and Laugesen, P. The interfacial transition zone (ITZ) between cement paste and aggregate in concrete. *Interface Science* 1`2, 411-421, Springer Netherlands (2004).

[47] Mondal, P., Shah, S. P. and Marks, L.D. Nanomechanical properties of interfacial transition zone in concrete. *Nanotechnology in Construction* 3, Springer, 315-320 (2009).

[48] Königsberger, M., Pichler, B. and Hellmich, Ch. Micromechanics of ITZ-aggregate interaction in concrete Part II: strength upscaling. *Journal of American Ceramic Society. Journal of American Ceramic Society* 97, 543-551 (2014).

[49] Kuhn, M.R. Structured deformation in granular materials. *Mechanics of Materials* 31, 407-442, 1999.

[50] Alonso-Marroquin, F., Vardoulakis, I., Herrmann, H.J., Weatherley, D. and Mora, P. Effect of rolling on dissipation in fault gouges. *Physical Review E* 74, 031306, 1-10 (2006).

[51] Skarżyński, Ł., Kozicki, J. and Tejchman, J. Application of DIC technique to concrete – study on objectivity of measured surface displacements. *Experimental Mechanics* 53, 1545-1559 (2013).

[52] Skarżyński, L. and Tejchman, J. Experimental investigations of fracture process in plain and reinforced concrete beams under bending. *Strain* 49, 6, 521-543 (2013).

[53] Bobinski, J. and Tejchman, J. Comparison of continuous and discontinuous constitutive models to simulate concrete behaviour under mixed mode failure conditions. *I. J. Num. Anal. Meth. Geomech.* (2014) (under review).

[54] Bobinski, J. and Tejchman, J. A coupled constitutive model for fracture in plain concrete based on continuum theory with non-local softening and eXtended Finite Element Method. *Finite Elements in Analysis and Design* (2014) (in review).